Quantifying the mechanisms of keyhole pore evolutions and the role of metal-vapor condensation in laser powder bed fusion

Tao Yu , Jidong Zhao [*]

Hong Kong University of Science and Technology, Clearwater Bay, Kowloon, Hong Kong

ARTICLE INFO

ABSTRACT

Key to quality control for laser powder bed fusion (L-PBF) is the reduction of porosity in built parts. However, understanding the mechanisms of a complete cycle of keyhole pore evolutions, including the processes of the keyhole pore generation, collapse, and splitting, and the role of metal-vapor condensation, remains a great challenge. In this study, we employ a high-fidelity computational tool considering multiphase interactions and thermal-induced phase changes to reproduce the key observations and identify the critical physics underlying keyhole instability and the ensuing keyhole pore generation, collapse, and splitting. We demonstrate that the dynamic fluctuation of keyhole and keyhole pores is dictated by five interdependent factors: vapor condensation, liquid vortex, recoil pressure, surface tension, and keyhole morphology. The occurrence of protrusions inside the keyhole wall enhances the fluctuation of keyhole by re-directing the reflected laser rays and changing the transport of high-temperature liquid flows surrounding the keyhole. The locally generated liquid vortex joins with the overall melt pool dynamics to snap the lower portion of a keyhole to form a keyhole pore and further drive its motion, conditions for which are quantified from the numerical results. We further show that vapor condensation is the major mechanism that may cause two high-speed microjets of pores and result in pore collapse and splitting. Finally, we propose an optimization strategy based on a parametric study of the condensation rate to potentially eliminate keyhole pores during laser melting.

1. Introduction

Laser powder-bed fusion (L-PBF) is emerging as a promising technology revolutionizing manufacturing for a wide range of engineering sectors and industries, including aerospace [1], biomedical [2–4], and defense industries [5]. It offers an economical and efficient pathway for printing complex-shaped parts without various constraints by design in conventional manufacturing industries [6–8]. Its future developments, however, hinge crucially upon improving the mechanical properties of the as-built parts by reducing detrimental defects [9,10] or applying a post-heat treatment [11]. The porosity of the fabricated parts, especially the keyhole-induced porosity in both laser welding [12] and L-PBF [13], is widely regarded as a major defect that can result in a reduction in ultimate strength, fatigue strength, and fracture strength [14–16]. Understanding the key mechanisms contributing toward the formation of pores in the keyhole mode melting has been a focus of recent research on L-PBF. A concerted effect has been made in both the research and manufacturing industries to explore various strategies to effectively reduce the porosity during the melting process [13,17,18].

In-situ high-speed X-ray imaging has become a popular experimental means to overcome the limitation of traditional *ex-situ* experimental approaches on L-PBF [6,19], which can only provide the pore features of as-built parts, such as the pore shape and position. It offers real-time, high-resolution observations of the dynamic processes in different stages of a typical melting process, including the keyhole evolutions [18, 20–24], spatter formation [25–27], and the formation [13,28] and elimination [29] processes of keyhole pores. Specifically, recent studies based on in-situ experiments show that significant fluctuations of the keyhole occur in keyhole mode melting [18, 30–32] and the instability at a moving keyhole tip contributes critically to the formation of keyhole pores [13,29]. Surface tension and melt flow have been identified as major factors driving the rapid, excessive, and often irregular deformation of the keyhole bottom observed [13]. The generated keyhole pore may further collapse and split [13], or shrink [28]. Zhao et al. [13] indicated that the impinging of a high-speed microjet on the opposite wall of the pore causes rapid pore collapse and splitting, and the vapor condensation may occur at the keyhole bottom as their image background becomes increasingly clear. Huang et al. [28] employed a bubble

model in consideration of the metal-vapor condensation. They found that the metal-vapor condensation in the enclosed keyhole pore may lead to the shrinkage and splitting of the keyhole pore. However, their bubble model is only capable of predicting the change of equivalent pore size while unable to model the pore splitting process and pore motion [28]. The role of vapor condensation on the keyhole pore shrinkage, collapse, or splitting remains unclear and unexplored. The thermo-mechanical dynamics, such as the acoustic waves and viscous drag, dominate the further movement of the keyhole pore [13, 18, 29, 33–35] in the melt pool. Despite the significant advances made in the field, the characteristics of keyhole instability and pore evolution remain largely based on observations and empirical interpretations. To date, their fundamental mechanisms have yet to be fully identified [10, 36–38]. It is of strong interest to understand the role of metal-vapor condensation on the microjet and the keyhole pore instability, the cyclic formation of a "J"-like keyhole pertaining to a collapsed keyhole pore, and the key mechanism governing pore motions.

Numerical modeling has been widely used as a complementary, cost-effective alternative to experimental approaches to explore the instability of keyhole and keyhole-induced pores [17, 36, 39–47]. Various advanced numerical approaches [10,48,49] have recently been developed to analyze the keyhole pore formation process and to explore optimal scan strategies or suitable environments to reduce the keyhole pores, such as the optimal combination of laser power [36,40,45], laser incident angle [44], laser energy density [41], and ambient pressure [17,42]. Previous simulations have placed a focus on the processes of keyhole pore formation and motion and the influencing factors, including laser power [17, 36, 40–45], incident angle [40], scanning speed [17,46], and ambient pressure [17] on these processes. Gaps remain in identifying other factors and their roles, such as the metal-vapor condensation in the keyhole pore and the processes of "J"-like keyhole formation, keyhole pore collapse and splitting, and motion of splitting pores. The entire life cycle of keyhole pores, including its collapse, splitting, and motion, and the role of metal-vapor condensation on the entire life cycle are highly dynamic processes that involve exceedingly complicated physics. To gain a comprehensive understanding of these processes, it is desirable and essential to develop a high-fidelity simulation framework that enables quantitative predictions consistent with in-situ experimental observations.

We employ herein a rigorous, physics-based computational approach [50,51] to examine the mechanisms governing the keyhole fluctuations and the formation, collapse, splitting, and motion of keyhole pores during a typical laser melting process. This study is intended to offer three innovative features as follows: (1) To help to reveal the mechanisms governing a complete cycle of typical keyhole and keyhole pore evolutions, including the processes of the "J"-like keyhole formation, the keyhole pore collapse and splitting, and the motion of splitting pores, that have not been previously fully discussed [17, 36, 39–47]. (2) To establish quantitative connections between vapor condensation and keyhole pore collapse and splitting, including the development of recoil pressure, surface tension, Marangoni's pressure, and velocity field around the keyhole pore, that cannot be directly obtained by in-situ or *ex-situ* experimental approaches [13,28]. (3) To systematically examine the effect of condensation rate on the keyhole pore and propose a possible optimization melting strategy through controlling the vapor condensation in the keyhole that has not been discussed in previous studies.

2. Methods

2.1. Multi-phase consideration of the melting process

The melting process of metal additive manufacturing involves multiple phases, including the solid metal, melt flow, metallic vapor, and ambient gas, and phase transitions among these different phases, such as melting, solidification, evaporation, and condensation. We have previously developed a high-fidelity, multi-phase, multiphysics computational framework based on fully resolved CFD coupled with DEM to tackle the challenges involved in the process [51]. The main focus of the current study is to understand the thermo-mechanical behavior of keyhole dynamics and the formation of pores in a bare plate, rather than investigating vapor-powder interactions. Therefore, the metallic vapor and the protective gas will not be distinguished and will be treated as a single ambient gas [17,41,44] in producing the keyhole depression in this study. The metallic vapor is considered to account for the mass transfer, recoil pressure, and latent heat during the keyhole motion. The solid metal is treated as a high-viscous fluid here for the convenience of numerical simulations [52]. The Darcy's term is incorporated in the momentum equation for modeling the solid state or partially melt state of the metal, which is commonly used in most existing literature [50, 52–54]. Therefore, the melting process of a bare plate subjected to laser illumination can be reasonably simplified as a solid-fluid two-phase problem in this study.

2.1.1. Volume of fluid method

We employ the volume of fluid (VOF) method in conjunction with a sharp interface capture scheme, isoAdevctor [55], to model the two-phase system involved in L-PBF. The isoAdevctor scheme helps to overcome the limitation of VOF, which can only obtain a smeared interphase between the metal and gas phases. This scheme offers a better-resolved interface than the default scheme in *OpenFOAM*, the MULES scheme [56], by adopting the iso-surface reconstruction to compute an accurate surface flux and a bounding procedure to limit the values of volume fraction within a specified range [56,57]. The computational fluid dynamics (CFD) with the VOF method is used to solve the fluid domain consisting of co-existing multiphase flows, including the solid metal, melt flow, and ambient gas.

2.1.2. Equivalent properties

In a multiphase CFD domain, the volume fractions of the metal and gas are denoted as α_1 and α_2, respectively, satisfying $\alpha_1 + \alpha_2 = 1$. The interface of the two phases to be solved by the VOF method refers to a region containing interface cells with a volume fraction (either α_1 or α_2) ranging from 0 to 1. The equivalent density ρ, equivalent viscosity μ, equivalent thermal conductivity k, and equivalent heat capacity C over the entire CFD domain could be written as:

$$\begin{cases} \rho = \alpha_1\rho_1 + \alpha_2\rho_2 \\ \mu = \alpha_1\mu_1 + \alpha_2\mu_2 \\ k = \alpha_1 k_1 + \alpha_2 k_2 \\ C = \alpha_1\dfrac{\rho_1}{\rho}C_1 + \alpha_2\dfrac{\rho_2}{\rho}C_2 \end{cases}, \tag{1}$$

where the subscripts (1 and 2) denote the metal phase and the gas phase, respectively.

2.2. Multi-way phase transitions

2.2.1. Melting and solidification

The melting and solidification processes are simplified as a dramatic viscosity change of the metal fluid between its solidus and liquidus temperatures. The following expression is employed to describe the change of metal viscosity μ with temperature [52]:

$$\ln\mu = \frac{1}{2}\text{erfc}\left[\frac{4}{\ln T_1 - \ln T_s} \bullet \left(\ln T - \frac{\ln(T_1) + \ln(T_s)}{2}\right)\right] \bullet (\ln\mu_s - \ln\mu_1) + \ln\mu_1, \tag{2}$$

Where μ_s and μ_1 are the viscosities at the solidus temperature T_s and liquidus temperature T_1, respectively. erfc() refers to the complementary Gaussian error function.

2.2.2. Evaporation

This study employs a recently proposed evaporation model [58] to calculate the mass loss rate, recoil pressure, and heat loss rate of the metal by evaporation. The evaporation model considers the gas-flow structure and material composition and is applicable for both common and near-vacuum environments [58]. It helps to overcome the limitation of the conventional Anisimov's evaporation model [59] in the near-vacuum environment. In this evaporation model, the mass loss rate $\dot{m}_v$, recoil pressure P_{re} and heat loss rate Q_v of the metal by evaporation at the common atmosphere are written as:

$$\dot{m}_v = -\left(1 - \frac{P_3}{P_e}\sqrt{\frac{T}{T_3}}\beta F^-\right)P_e\sqrt{\frac{M}{2\pi RT}}, \tag{3}$$

$$P_{re} = \frac{e^{D^2}}{2}\left(2D^2 + 1\right)\left(F^- + \sqrt{\frac{T_3}{T}}G^-\right)P_e, \tag{4}$$

$$Q_v = \dot{m}_1 L_v, \tag{5}$$

where T is the temperature of the liquid surface. P_e is the saturated vapor pressure. P_3 and T_3 are the pressure and temperature out of the Knudsen layer [60], respectively. M is the molar mass and R is a universal gas constant. L_v is the latent heat of evaporation. D, F^- and G^- are dimensionless variables related to the ratio of isochoric and isobaric specific heat capacity of the gas and the Mach number out of the Knudsen layer [58].

2.2.3. Condensation

Gas condensation may cause the collapse of a closed pore surrounded by liquids [61]. In this study, the vapor condensation in the closed keyhole pore is considered to understand the mechanism of the collapse and splitting of keyhole pores. Specifically, Badillo's condensation model [62–64] is used to calculate the condensation rate of the vapor.

$$\dot{m}_c = \frac{6\sqrt{2}}{5}\frac{k_1(T - T_b)}{wL_v} \tag{6}$$

where k_1 is the heat conductivity of the metal, T_b is the boiling temperature, L_v is the latent heat of evaporation, and w is the characteristic length of the interface which is approximated by the height of the CFD cell [64].

2.3. Laser absorption model

The laser absorption model is built based on the VOF-compatible ray-tracing model we recently proposed [51]. This model considers the Fresnel reflection and refraction at the metal surface and the laser attenuation and absorption in the metal. The model is further enhanced in this study to take into account the effect of the metal state on the attenuation distance and the effect of the surface temperature on the laser reflectivity. Specifically, the absorption coefficient of the solid metal α_s can be calculated from Swanepoel method [65] using the extinction coefficient k_e and the laser wavelength λ, i.e., $\alpha_s = 4\pi k_e/\lambda$. The absorption coefficient of the liquid metal α_l is obtained from our previous work [51]. The reflectivity of aluminum (Al) [66] is adopted here due to the unavailability of reliable experimental data for Ti-6Al-4 V. The following equation shows the reflectivity change from the room temperature to the liquidus temperature.

$$f_R = \frac{1}{2}\text{erfc}\left[\frac{4}{T_1}\bullet\left(T - \frac{T_1}{2}\right)\right]\bullet(f_{Rl} - f_{R0}) + f_{R0}, \tag{7}$$

where T is the temperature, T_1 is the liquidus temperature, f_{Rl} and f_{R0} are the reflectivity at the liquidus temperature and 0 K, respectively.

2.4. Governing equations

Three sets of governing equations describing the multiphase, multiphysics processes of laser melting are solved by CFD implemented with the aforementioned models pertaining to melting and solidification, evaporation, condensation, and laser absorption. They include the advection equation for the volume fraction field of two fluid phases, the fluid momentum equation based on the Navier-Stokes equation for the flow dynamics, and the temperature equation for the thermal field.

2.4.1. Advection equation

In this study, we consider the metal phase with two interphase mass transfer rates $\dot{m}_v$ and $\dot{m}_c$, representing respectively the vaporization of the liquidus metal into the metallic vapor and the condensation of the metallic vapor into the liquidus metal. Both the metal and the gas phases are assumed to be incompressible and are solved by the following advection equation,

$$\begin{cases} \dfrac{\partial\alpha_1}{dt} + \nabla\bullet(\alpha_1\mathbf{u}) = \dfrac{2\alpha_1\dot{m}_v - 2\alpha_2\dot{m}_c}{\rho_1}|\nabla\alpha_1|, \\ \alpha_2 = 1 - \alpha_1 \end{cases} \tag{8}$$

where $\mathbf{u}$ is the velocity. α_1 and α_2 represent the volume fractions of the metal and the gas, respectively. $|\nabla\alpha_1|$ is an interface term to transform a surface term per unit area into a volumetric term [67–69]. $2\alpha_1$ or $2\alpha_2$ is a sharp surface term to smear out the interphase [70].

2.4.2. Momentum equation

The flow dynamics of two fluid phases during the laser melting are assumed to be governed by the following momentum equation based on the Navier-Stokes equation. We consider terms accounting for multiple physical phenomena, including the surface tension, Darcy's effects, recoil pressure, and Marangoni's flow, as shown in the RHS of the following equation. Specifically, the Darcy's term describes energy dissipation in a mushy zone with partially melted metal [50, 52–54]. The recoil pressure is caused by the evaporation of melt flow [71]. The Marangoni's flow considers the change of surface tension with the temperature gradient in the melt [72].

$$\begin{aligned}\frac{\partial}{\partial t}(\rho\mathbf{u}) + \nabla\cdot(\rho\mathbf{u}\otimes\mathbf{u}) = & -\nabla p + \nabla\cdot(\mu\cdot(\nabla\mathbf{u})) + c\sigma|\nabla\alpha_1|\frac{2\rho}{\rho_1 + \rho_2}\mathbf{n} \\ & -K_c\frac{(\alpha_1 - \alpha_m)^2}{\alpha_m^3 + C_k}\mathbf{u} + P_{re}|\nabla\alpha_1|\frac{2\rho}{\rho_1 + \rho_2}\mathbf{n} \\ & +\frac{d\sigma}{dT}(\nabla T - \mathbf{n}(\mathbf{n}\cdot\nabla T))|\nabla\alpha_1|\frac{2\rho}{\rho_1 + \rho_2} \end{aligned} \tag{9}$$

where p is the pressure and $p = p_d + \rho gh$. p_d is the dynamic pressure, g is the gravitational acceleration, and h is the reference height [52]. K_c is the permeability coefficient, C_k is a constant to avoid division by zero. α_m is the volume fraction of the molten metal which can be approximated using a Gaussian error function [52]. C is the curvature of the metal-gas interface, and $c = -\nabla\bullet\mathbf{n}$. $\mathbf{n}$ is the unit normal vector at the interface, and $\mathbf{n} = \nabla\alpha_1/|\nabla\alpha_1|$. $2\rho/(\rho_1 + \rho_2)$ is a sharp surface force term to smear out the interphase [67,70]. T_s is the solidus temperature. $d\sigma/dT$ represents the change of surface tension coefficient σ with temperature. The volume fraction of the molten metal α_m and the surface tension coefficient σ [52] can be written as:

$$\alpha_m = \frac{\alpha_1}{2}\left[1 + \text{erf}\left(4\left/(T_1 - T_s)\left(T - \frac{T_1 + T_s}{2}\right)\right.\right)\right], \tag{10}$$

$$\sigma = \begin{cases} \dfrac{\sigma_1}{1 + \text{erf}2}\left[1 + \text{erf}\left(\dfrac{4}{T_1 - T_s}\left(T - \dfrac{T_1 + T_s}{2}\right)\right)\right] & T \leq T_1 \\ \sigma_1 + \dfrac{\partial\sigma}{\partial T}T & T > T_1 \end{cases}, \tag{11}$$
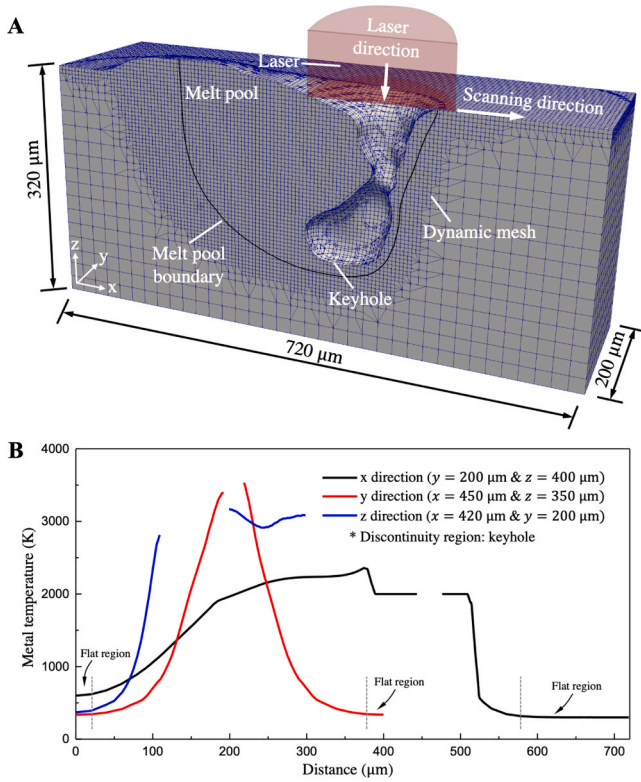
Fig. 1. Model setup. (A) Multiphase, multiphysics simulation of laser melting of a bare Ti-6Al-4 V plate: half simulation domain, discretization, laser and scanning directions, and dynamic meshing of critical subdomains surrounding the melt pool. (B) The change of metal temperature along three typical directions of x, y, and z, respectively. The interruption with the curve represents the keyhole. "$y = 200\mu m$ and $z = 400\mu m$" means the intersection of the section $y = 200\mu m$ and the section $z = 400\mu m$.

where σ_l is the surface tension coefficient of the metal at the liquidus temperature.

2.4.3. Temperature equation

The thermal field is governed by the following temperature equation derived from the energy conservation. The seven terms on the RHS of the temperature equation represent heat transfers due to laser heat, conduction, dissipation, fusion, convection, radiation, and vaporization [52], respectively,

$$
\begin{aligned}
\frac{\partial(C\rho T)}{\partial t} + \nabla(C\rho T)\cdot \mathbf{u} &= S_l + \nabla\cdot(k\nabla T) + \mu(\nabla\mathbf{u} + \mathbf{u}\nabla):\nabla\mathbf{u} \\
&- L_f\left[\frac{\partial}{\partial t}(\rho\alpha_m) + \nabla\cdot(\rho\mathbf{u}\alpha_m)\right] - h_c\left(T - T_{ref}\right)\left|\nabla\alpha_1'\right|\frac{2C\rho}{C_1\rho_1 + C_2\rho_2} \\
&- \sigma_{sb}\left(T^4 - T_{ref}^4\right)\left|\nabla\alpha_1'\right|\frac{2C\rho}{C_1\rho_1 + C_2\rho_2} - Q_v\left|\nabla\alpha_1'\right|\frac{2C\rho}{C_1\rho_1 + C_2\rho_2}
\end{aligned}
$$
(12)

where L_f is the latent heat of fusion, h_c is the convective heat transfer coefficient, T_{ref} is the reference temperature, and σ_{sb} is the Stefan-Boltzmann constant. S_l is the laser input obtained from our previous VOF compatible ray-tracing model [51] with a modified reflectivity and absorption coefficient described in the laser absorption model.

2.5. Implementation of the proposed method

The computational approach employed in this study pertains solely to the CFD component of the multiphase semi-coupled resolved CFD-DEM [50,51]. This approach has been implemented in two

open-source codes, namely OpenFOAM and LIGGGHTS, with further enrichments on a coupling engine called *CFDEM*. The complete implementation strategies of the multiphase semi-coupled resolved CFD–DEM and relevant benchmarks for validating the thermodynamics, vapor-particle interactions, and ray-tracing model can be found in references [50,51]. The solution procedure for the computational approach used in this work is summarized as follows:

(1) Prescribe the initial conditions for the CFD domain, including the volume fraction field, temperature field, pressure field, and velocity field of fluids.
(2) Calculate the absorbed laser energy based on the ray tracing model [51] that considers the effect of the metal state on the attenuation distance and the effect of the surface temperature on the laser reflectivity. The detailed implementation procedure of the ray tracing model can be found in our previous work [51].
(3) Solve the temperature equation (Eq. (12)) that considers the laser energy, six heat transfer terms due to dissipation, conduction, convection, radiation, fusion, and evaporation.
(4) Update the mass transfer ratio (Eq. (6)) based on the new temperature field and solve continuity equations in Eq. (8) using isoAdvector scheme [55] to update the volume fraction field. The detailed implementation strategy of the VOF method in conjunction with the isoAdvector scheme can be found in the reference [55].
(5) Update physical parameters in Eq. (1) according to the volume fraction field and temperature field, including density, heat capacity, thermal conductivity, and viscosity.
(6) Update the velocity field $\mathbf{u}_f$ and pressure field p_0 by solving the momentum equation in Eq. (9) that considers the surface tension, Darcy's effects, Marangoni's flow, recoil pressure, and gravity. Pressure Implicit with Splitting of Operators (PISO) algorithm [73] is applied here to solve the velocity and pressure iteratively.
(7) Go to Step (2) to repeat the simulation until the final time step is reached.

2.6. Method validation

In our previous works [50,51], we have provided multiple benchmark cases, including the morphology of melt track, laser absorption, melt pool shape, and powder motion, to validate the computational tool. In this study, four additional benchmark cases are presented in Appendix A, namely Marangoni's flow, solid melting, two-phase model, and evaporation model, to further validate the computational tool. As these four benchmark cases are fundamental and well-established, we have only provided simulation results in the appendix to avoid excessive distraction of the focus of the study. The detailed information used for benchmark cases, such as the model setup and physical parameters, can be found in the literature by Salid [74] (Cases I to III) and Cunningham [18] (Case IV). The quantitative comparisons between simulation and experimental results shown in "Appendix A" offers rigorous validations of the proposed computational tool.

3. Results and discussion

3.1. Model setup and parameter selection

3.1.1. Model size and relevant parameters

The laser melting process of a bare Ti-6Al-4 V plate is simulated with the computational framework described above to study the instability mechanisms of the keyhole and keyhole pore. We choose a specific laser case with a laser spot size of 100 μm, a laser power of 205 W, and a scanning speed at 500 mm/s as described in the literature [13]. A Ti-6Al-4 V plate of $720 \times 400 \times 320$ μm in dimension, as shown in half from the center cross-section of the width direction in Fig. 1A, is considered. The laser is assumed to move along the longest dimension
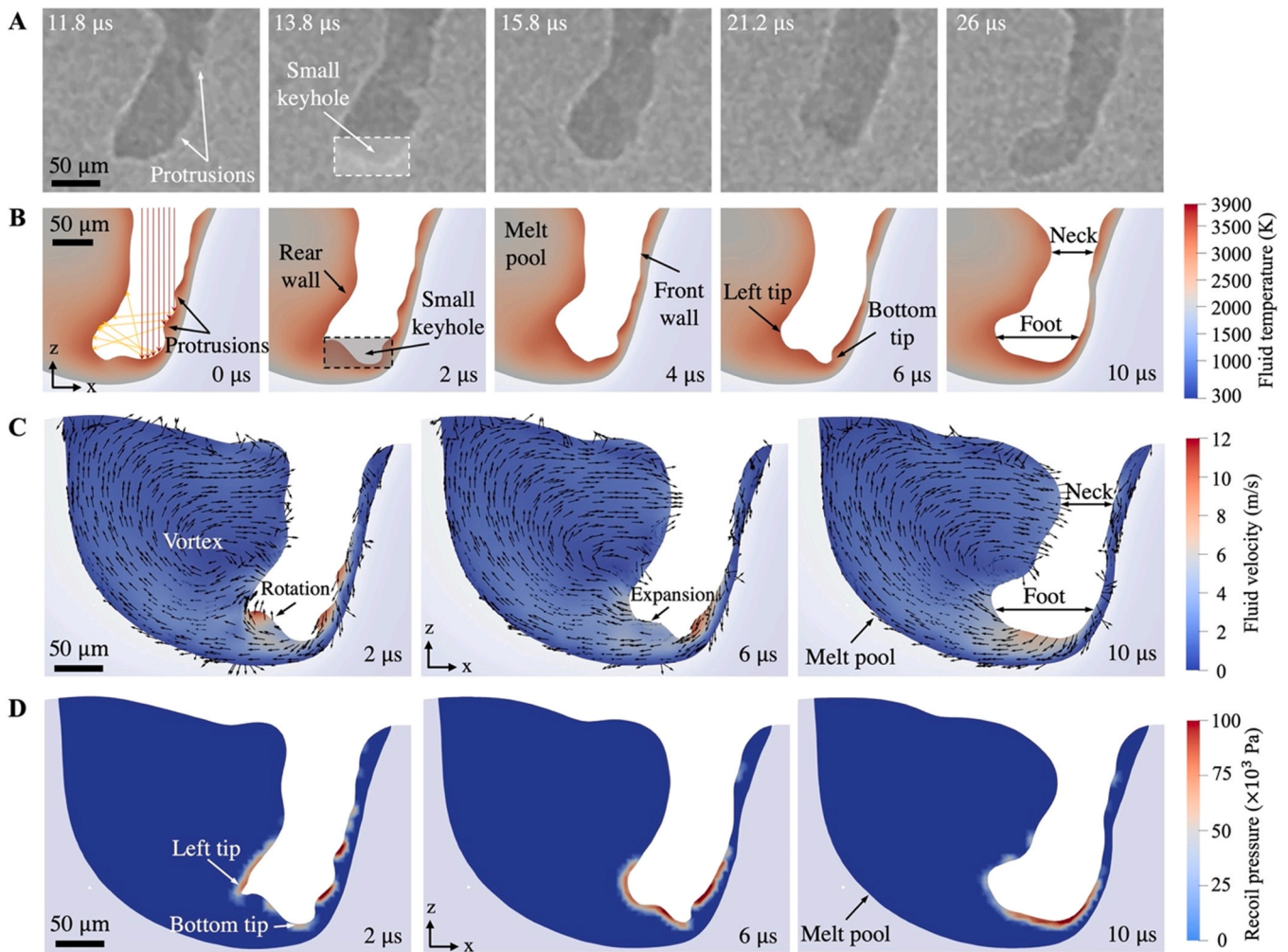
Fig. 2. Formation of "J"-like keyhole. (**A**) Megahertz x-ray images captured from the supplementary movie S12 in the literature [13]. (**B**) Central cross-section profile of the simulated keyhole in terms of temperature contour at $y = 200$ μm. The incident rays and 1st reflected rays in the keyhole at 0 μs are schematically illustrated using red and yellow lines, respectively. (**C** and **D**) Simulated velocity vector contour (C) and recoil pressure contour (D) of the central cross section at $y = 200$ μm. More time instances can be found in "Appendix C".

(720 μm), which is set to be the *x* direction. The width and depth directions are set as the y-direction or z-direction, respectively. Relevant constant physical parameters [17,50] and temperature-dependent thermal parameters [75] adopted in the simulations are summarized in "Appendix B".

3.1.2. Setup of mesh, time step and boundary condition

Dynamic meshing is applied in the study to improve computational efficiency. As shown in Fig. 1A, coarse meshes are initially used to discretize the entire CFD domain and will be adaptively refined in specific regions satisfying $|\nabla \alpha_1| \rangle 0$, $T > 1000$ and $S_l > 0$, where α_1 is the volume fraction of metal, T is the temperature, and S_l is the absorbed laser energy. A region with a dense mesh will be further updated in each time step if necessary. In this study, the grid size of the coarse mesh is 20 μm, and the grid size of the dense mesh is 5 μm based on the benchmarks in our previous work [51]. The time step is 1×10^{-7} s. The bottom boundary is set as a non-slip wall with a zero gradient for pressure and temperature. Other boundaries are set to a fixed value for pressure and a zero gradient for velocity and temperature. Fig. 1B shows the temperature change along the three representative directions of x, y, and z, confirming the prescribed boundary condition of temperature to be reasonable.

3.1.3. Assumptions on vaporization and condensation

Note that, the metallic vapor and the protective gas are treated as a single phase (ambient gas) [17,41,44] in this study. The effect of vaporization on the keyhole is considered by taking into account the mass loss, recoil pressure, and latent heat of the metal by vaporization [58] (More details are documented in the "Multi-way phase transitions" section in the Methods). To further examine the impact of vapor condensation in the keyhole pore, we assume that the vapor is uniformly distributed in a keyhole pore. The condensation duration is assumed to be the same as the duration of the keyhole pore collapse and splitting observed in the experiment [13], i.e., 4.6 μs, after which only incompressible protective gas is left in the enclosed keyhole pore. The condensation rate is calculated by Eq. (6) in the "*Multi-way phase transitions*" section. The vapor condensation in an enclosed keyhole pore may generate a pressure drop according to the ideal gas equation of state, leading to potential pore deformation. In this study, we only consider vapor condensation in the enclosed keyhole pore but ignore the vapor condensation in the keyhole connecting with the ambient gas.

3.1.4. Pros and cons of CFD models with vapor plume capability

The inclusion of the vapor plume in advanced CFD simulations of L-PBF provides two major advantages in terms of simulation accuracy. First, the high-speed vapor plume escapes from the melt pool and entrains surrounding ambient gas and powders [76,77], contributing to
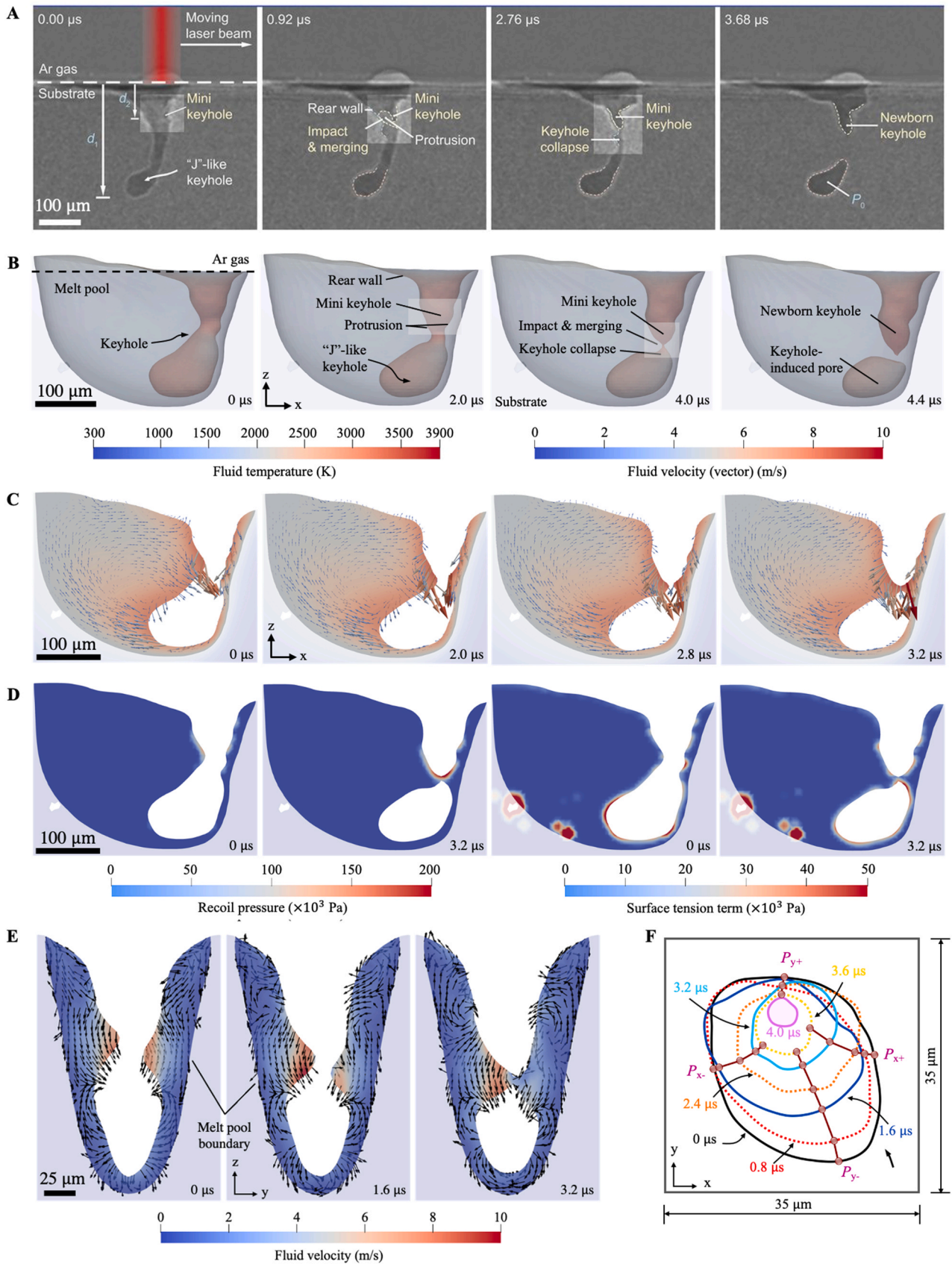
Fig. 3. Keyhole pore formation. (**A**) Megahertz x-ray images of a keyhole pore-formation process [13]. (**B**) Simulated keyhole pore-formation process. (**C**) Temperature contour and velocity vector contour of the central section at $y = 200$ μm. (**D**) Contours of the recoil pressure (left) and surface tension term (right) of the central section at $y = 200$ μm. The surface tension term means the equivalent pressure caused by the surface tension for better comparison with the recoil pressure. (**E**) Velocity vector contour of the section at $x = 450$ μm. (**F**) Keyhole neck morphology contour in the xy-plane.

possible sparking and scattering of powder grains. This physical process causes possible defects to the final print part [78,79], such as lack of fusion, pores, inclusion, balling, and rough surfaces [80–83]. Considering the vapor plume in the simulations allows for the capture of vapor-powder interactions and the revelation of inherent mechanisms of defect formation [37,51,84]. Second, using a physics-based distribution of the vapor plume in the keyhole, instead of the uniform distribution assumption, enhances the accuracy of the condensation model in the CFD simulations. Nevertheless, the tradeoff is the resulting high computational cost in adopting plume modeling in the CFD simulations. Indeed, the vapor plume may experience high speeds greater than 100 m/s [37,84] and can even reach 700 m/s with higher laser energies [76]. Due to the high-speed vapor plume, a smaller time step and a larger CFD domain with finer meshes enabled by dynamic meshing are required, which would remarkably increase the computational cost to at least six times greater than that without considering the vapor plume [51].

3.1.5. Feasibility of assumptions

The numerical simulations in this study are based on two major assumptions. First, this study ignores the powder bed, as it only has a secondary influence on the deep keyhole formation and the generation and deformation of keyhole pores in L-PBF [18]. Furthermore, the non-uniform deposition of powders and relevant powder motion during the L-PBF process may significantly increase the difficulty and complexity of studying the effect of vapor condensation on keyhole pore instability. Second, the study employs simplified evaporation and condensation models without considering the vapor plume. This is acceptable because the significant effect of vapor plume on powders can be ignored in this case with a bare plate. The effect of vapor distribution in the keyhole pore can be further studied by a parametric analysis with systematically adjusted condensation rates. Overall, these two assumptions help us fetch a balance between computational cost and efficiency.

3.1.6. Research objectives in this study

In what follows, a complete cycle of typical keyhole and keyhole pore developments, including the "J"-like keyhole formation and fluctuation, and the generation, collapse, splitting, and motion of keyhole pore, is simulated and examined against experimental observations. Quantitative discussions are devoted to various key aspects of the keyhole and keyhole pore, including their morphological evolutions, liquid speed, and thermo-mechanical forces. We further perform a parametric study on the condensation rate to study its effect on the keyhole pore deformation and motion, based on which a possible optimization strategy by controlling the condensation rate to eliminate keyhole pores is proposed. All cases included in this study were executed on the Tianhe II National Supercomputer in Guangzhou with 36 processors and 180 GB memory, and each case required two days to complete. New mechanisms governing the instabilities of keyhole and keyhole pores are identified based on rigorous analyses of the results, revealing some different insights from previously proposed speculations [13].

3.2. Formation of "J"-like keyhole: dynamic features at keyhole bottom

Keyhole pores are frequently found to emerge when the bottom tip of a "J"-like keyhole is pinched off, as confirmed by in-situ high-speed X-ray imaging [13]. A particular recent research focus is to understand the mechanism of pore formation relevant to the dynamic evolution of a "J"-like keyhole [17,44]. Fig. 2 shows a comparison of the typical formation process of the "J"-like keyhole captured by in-situ high-speed X-ray imaging [13] (Fig. 2A) and our numerical simulations (Fig. 2B), showing a qualitative resemblance between the two. In particular, in both the experimental video [13] and our numerical simulations, we identify an interesting feature of reiterative two-stage development at the bottom of a "J"-like keyhole. The overall formation of a 'J'-like keyhole can be attributed to the reiterative two-stage development,

which we coin herein as the local rotation and the global expansion, respectively. The two stages are highlighted in Fig. 2 (A to C). The development of these two stages is a result of multiple interconnected physics involving laser absorption, protrusions of the keyhole wall, vortex flow, and recoil pressure, as detailed below.

3.2.1. Local rotation towards the "J" toe

The dynamic process at the bottom of the "J"-like keyhole is first characterized by a recurrent local rotation at the left tip of the keyhole (or "J" toe hereafter) in the wake of the occurrence of "small keyhole" (see second panels of Fig. 2A & B and first panels of Fig. 2C & D). Its mechanism is explained in connection with Fig. 2 as follows. The fluctuating nature of the front wall keyhole, when subject to laser illumination, leads to a nonuniform temperature distribution and hence multiple protrusions along the front wall (see 11.8 μs in Fig. 2A and 0 μs in Fig. 2B). These protrusions change the direction of the reflected laser rays that reach the bottom of the keyhole, which further cause nonuniform laser absorptions and evaporations at the bottom. The resultant recoil pressure causes the drilling of the bottom tip and forming the small keyhole, as shown in the panels of 13.8 μs in Fig. 2A and 2 μs in Fig. 2B. A local vortex flow, akin to the clockwise global vortex in the melt pool, is generated in the small keyhole. It further pushes the rotation of melt flow clockwise along the keyhole bottom, leading to an apparent local rotation mechanism (see the flux flow in 2 μs of Fig. 2C).

3.2.2. Transition from local rotation to global expansion at the keyhole bottom

The local rotation at the "J" toe of the keyhole is followed by an overall expansion of the keyhole bottom. Two contributing factors drive the transition. One is associated with an increase in energy absorbed by the keyhole bottom. When the protrusions along the front wall of the keyhole move down to merge with the keyhole bottom, the keyhole bottom receives more direct and reflected rays. The other is relevant to the dynamic flow and heat transport. The local rotation and the protrusions with a velocity $|\mathbf{u}|$ exceeding $10\,\text{m/s}$ shown in Fig. 2C help to transport the high-temperature liquid to both the left tip and the bottom tip. In particular, the protrusion in the front wall always concentrates the laser energy [85], causing a high temperature and a large recoil pressure (Fig. 2D). The rapid downward movement of the high-temperature protrusion accelerates the temperature rise at the bottom tip and enhances its rotation, which further facilitates the transport of more high-temperature fluid through the keyhole bottom to the left tip. As a result of both processes, the global temperature of the keyhole bottom increases quickly to cause its overall expansion, generating a strong vortex in the surrounding melt pool with a velocity $|\mathbf{u}|\rangle 5\,\text{m/s}$. The bottom vortex further merges and strengthens the global vortex in the melt pool and shrinks the keyhole neck, leading to a "J"-like keyhole.

3.3. Keyhole instability, necking and pore formation

Elevated levels of porosity in produced parts invariably lead to poor elastic modulus, yield strength, tensile strength, and elongation at fracture [86–89]. Porosity under keyhole mode melting is a common defect in L-PBF [18,20], and has garnered significant attention [31,90,91] among various pore defects. Keyhole closure and surface tension are considered as dominant reasons for the formation of a keyhole pore [13,17,44]. To gain new insights into this issue, we numerically reproduce the generation of a keyhole, as observed in experiments [13].

3.3.1. Comparison between simulation and experimental results

Fig. 3 (A and B) show a reasonable, consistent comparison of the experimental observations with numerical simulations on the pore generation process. Notably, there are discrepancies between the current numerical simulations and the experimental observations [13] on
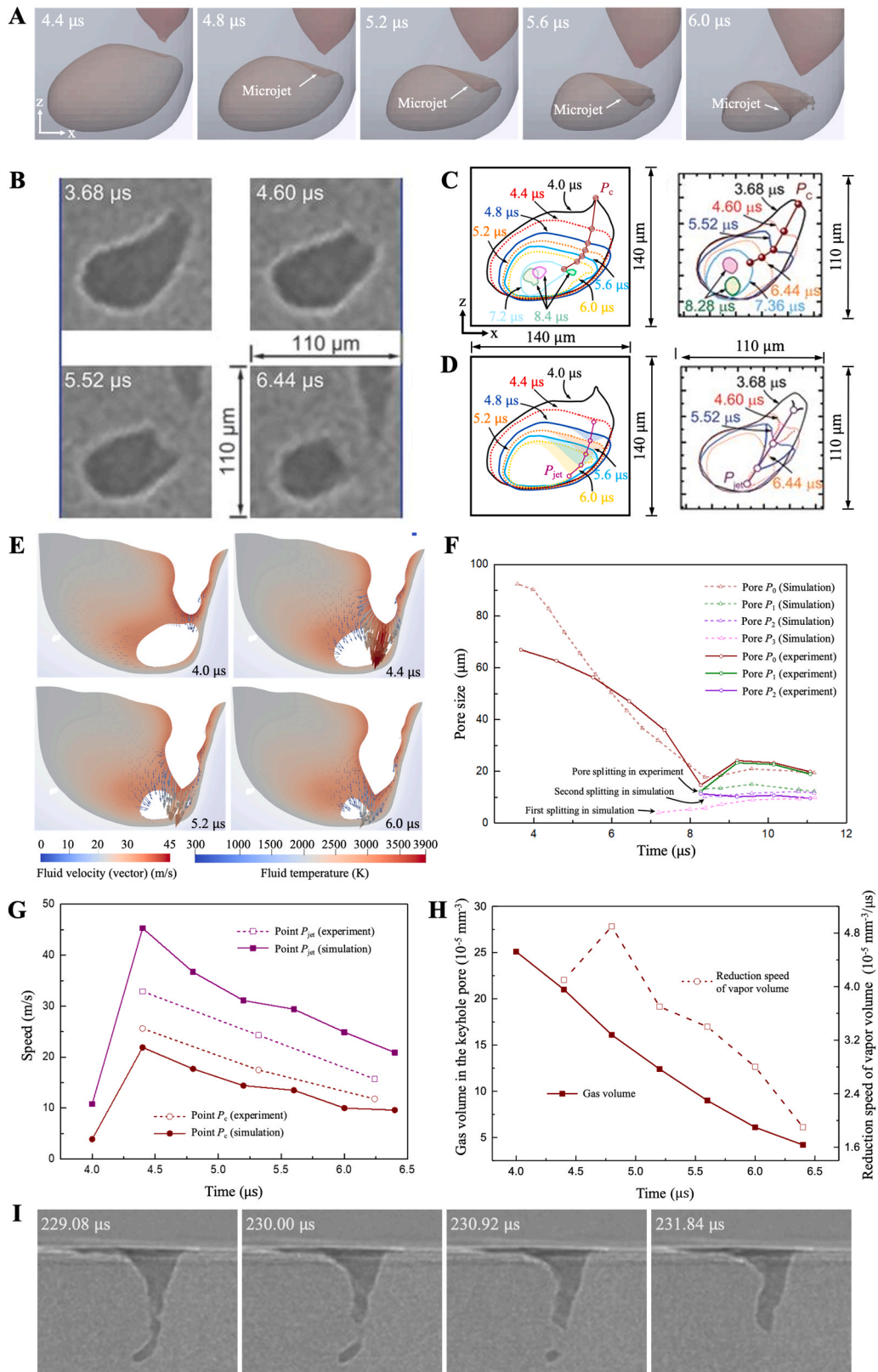
Fig. 4. The dynamics of keyhole pore collapse in the *xz*-plane. (**A**) Simulated microjet penetrating the keyhole pore. (**B**) Megahertz x-ray images showing the nonuniform collapse driven by a microjet [13]. (**C** and **D**) Comparison of the pore (**C**) and microjet (**D**) morphology contours between simulation (left) and experimental results (right) [13]. (**E**) Contours of temperature and velocity vector in the section at $y = 200$ μm. (**F**) Comparison of the equivalent pore diameter estimated from (**C**) between simulation and experimental results [13]. (**G**) Comparison of the speeds of Point P_c and Point P_{jet} between simulation and experimental results [13]. (**H**) Gas and vapor volume changes in the closed keyhole pore. (**I**) Megahertz x-ray images of keyhole pore collapse and elimination, captured from the supplementary movie S11 in the literature [13].

the size and speed of the protrusion in the front keyhole wall, due probably to the selection of some of the physical parameters, such as the laser reflectivity and absorption coefficient. Nevertheless, based on both the latest simulation results [17] and the current simulation results, there are cases where the speed and size of the protrusion in the front wall are not significantly larger than those in the rear wall. It leads to a head-on collision of the protrusions of the two keyhole walls to enclose the keyhole and generate a keyhole pore. It is evident from Fig. 3C that the steady decrease of the keyhole neck is driven by the vortex flow in the melt pool behind the keyhole back wall. The pre-closing process is rather similar to the "J"-like keyhole-formation process in Fig. 2. Continuous developments of protrusions in both the rear and front keyhole walls further accelerate the necking process to form a keyhole pore. A larger protrusion can significantly shorten the depth of the newborn keyhole as compared to our simulation results, as shown in Fig. 3 (A and B).

3.3.2. Effect of surface tension and recoil pressure on keyhole instability

The keyhole instability occurs under the influence of both the necking of protrusions and the motion of the mini keyhole, as shown in Fig. 3B, while the lower portion of the keyhole remains largely stable under the vortex flow in the melt pool. The physical mechanism of keyhole instability can be better explained using the distribution of the recoil pressure and surface tension on the keyhole depression surface, as presented in Fig. 3D. Note that the Marangoni's pressure is not presented since its maximum is only one-twentieth of that of the recoil's pressure and one-fifth of the maximum equivalent pressure caused by the surface tension in both the mini keyhole and keyhole pore. As shown in Fig. 3D, at 0 μs, only limited recoil pressure is found acting on the keyhole bottom while it is primarily stabilized by the surface tension with an equivalent pressure greater than 30 kPa. The recoil pressure, however, plays a dominant role in the mini keyhole and the newborn keyhole. Its maximum value reaches over four times larger than the equivalent pressure caused by the surface tension. After 0 μs, the two protrusions in the mini keyhole are driven by the recoil pressure to move downward continuously. Facilitated by the vortex in the melt pool, the left protrusion in the rear wall moves obliquely downward with a velocity larger than 6 m/s and becomes closer to the front wall. Since the front keyhole wall is an inclined surface, the right protrusion in the front wall, driven by the recoil pressure, also moves obliquely downward to the left protrusion with a velocity larger than 8 m/s. The two protrusions collide and merge at 2.76 μs in the experiment and at 4 μs in our simulation results, as shown in Fig. 3 (A and C). At 3.2 μs, obvious surface tension with an equivalent pressure over 50 kPa appear on the top-right corner of the closed pore. It plays a role in minimizing the surface area [44] and stabilizing the generated keyhole pore.

3.3.3. Keyhole morphology evolution in the yz-plane

Fig. 3E further shows a side view of the keyhole morphology evolution at the cross section cut through $x = 450$ μm. The protrusions in both lateral sides of the keyhole wall are driven by a high recoil pressure and move towards each other rapidly before they collide. There is a significant velocity reduction occurring from the protrusion to the adjacent melt pool boundary due to the large drag force from the mushy zone [17]. Therefore, only two protrusions move downwards obviously compared with other portions of the melt pool close to the melt pool boundary in this section and collide with each other. It is evident that the protrusions are asymmetric and move at different speeds. The right protrusion is farther away from the laser center and moves slower due to the less absorption of laser energy and hence smaller recoil pressure. However, the left protrusion is close to the laser center and travels at a higher speed to meet the slow right protrusion at a collision position to the right of the laser center.

3.3.4. Keyhole neck evolution in the xy-plane

We further use the evolving contour of the keyhole neck in the *xy*-

plane in Fig. 3F to demonstrate that the slower protrusion indeed determines the keyhole closure process. P_{y+} denotes the protrusion farther away from the laser center (the right protrusion in Fig. 3E), which has the lowest moving speed among the four. It serves as an anchor or converging point which remains largely stationary during the entire keyhole closure process while waiting for the other three protrusions to approach and merge with it. Note that such an asymmetrical closing process will help to produce an irregularly shaped, asymmetric keyhole pore and further affects the subsequent keyhole pore-splitting process.

3.4. Keyhole pore collapse

The collapse of keyhole pore with a high-speed microjet has been confirmed by high-speed x-ray imaging [13], as shown in Fig. 4B. Zhao et al. [13] found that the impact and merging of the keyhole walls at a horizontal speed of ~13 m/s create a high-speed microjet, and the vapor condensation may occur at the keyhole bottom as the image background becomes increasingly clear. Note that the proposed physical interpretation has been based on 2D megahertz x-ray images. It remains interesting to explore the inherent mechanisms governing the keyhole pore collapse and high-speed microjet [28].

3.4.1. Three arguments for the role of vapor condensation

There are three significant aspects that vapor condensation may become a critical factor affecting the collapse of a keyhole pore. (1) A rapid volume reduction of the gas phase confined in the keyhole pore is frequently observed to occur during the keyhole pore-collapse process, as shown in Fig. 4I and supplementary movies S11 and S12 in the literature [13]. As is widely known, however, the argon gas and metallic vapor at a velocity smaller than one-third of the sound speed can be largely regarded as incompressible gas [92]. Indeed, experimental observations on the elimination of a keyhole pore, as shown in Fig. 4I suggest the inclusion of other significant factors, including vapor condensation, may provide a reasonable explanation of the phenomenon. (2) A latest study [28] further employed a bubble model in consideration of the metal-vapor condensation to predict the equivalent pore size during the shrinkage and splitting processes of keyhole pore in SLM, yielding rather consistent predictions on the keyhole pore size with experimental observations. (3) The keyhole bottom, shadowed by the protrusions, stops absorbing the incident laser energy directly and hence experiences a quick temperature drop [93]. The temperature in this region keeps decreasing during the keyhole pore formation process due to the continuous growth and collision of protrusions, providing a driving force for vapor condensation in an enclosed keyhole pore.

To identify the role played by vapor condensation in the collapse and splitting of a keyhole pore, a systematic numerical investigation is performed in the following with rigorous comparison against experimental observations. Our high-fidelity multiphase, multi-physics computational framework [51] enables a rigorous consideration of vapor condensation, providing a pathway to explain its relevance to the underlying mechanisms accounting for the various intricate phenomena.

3.5. Key role of vapor condensation on keyhole pore collapse

The simulated pore collapse process is compared with experimental observations in Fig. 4, showing a reasonable overall consistency. Fig. 4A shows the simulated microjet development and the impinging of the microjet on the opposite wall of the keyhole pore during the pore-collapse process, in comparison with the experiments in Fig. 4B. The microjet forms a concave surface of liquid metal over its occupied portion of the keyhole pore. The difference in material renders the microjet identifiable by high-speed x-ray imaging. Fig. 4C and D present a side-to-side comparison of the simulated morphologies of the keyhole pore and the microjet marked with the trajectories of the top-right edge of pore P_c and the microjet tip P_{jet} with experimental results, showing rather good agreements. Fig. 4F and G further show a consistent trend of
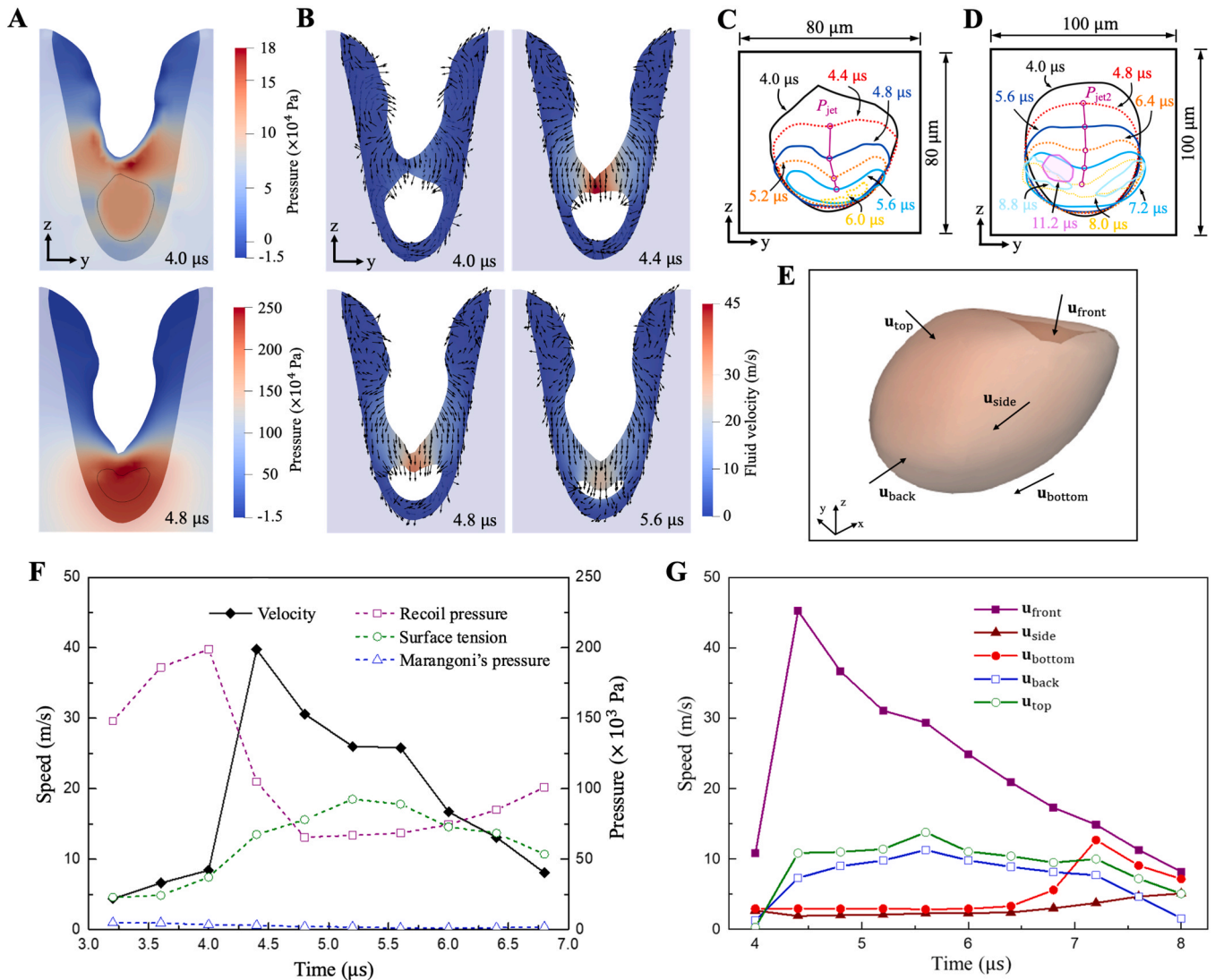
Fig. 5. The dynamics of keyhole pore collapse in the *yz*-plane and around the keyhole pore. (**A**) Pressure contour of the keyhole pore and surrounding fluids in the section at $x = 450$ μm. The area within the black line represents the keyhole pore. (**B**) Velocity vector contour in the section at $x = 450$ μm. (**C** and **D**) Pore morphology contour in the section at $x = 450$ μm (c) and $x = 400$ μm (D). (**E**) Velocity, recoil pressure, surface tension, and Marangoni's pressure at the newborn keyhole tip. (**F**) Schematic of five typical velocities at the front, top, side, bottom and back of the keyhole pore at 4.8 μs. (**G**) Variations of the five typical velocities indicative in (F) from 4 μs to 8 μs. Notes: the section at $x = 450$ μm passes through the newborn keyhole tip at 4.4 μs. The section at $x = 400$ μm passes through the center of Pore P_2 at 8.4 μs.

equivalent pore size and traveling speed of the two points, P_c and P_{jet}, during the collapsing process of the pore. There are discrepancies between the experimental and simulated results in terms of equivalent pore size and point speeds, especially at the beginning of vapor condensation. The discrepancies reflect a combined influence of a larger initial pore size and a simplified condensation model employed in this study.

3.5.1. Speed evolution and trajectory of P_{jet} and P_c

The vapor condensation in the closed keyhole pore causes a rapid reduction of pore size and gas volume, as shown in Fig. 4F and H. It further leads to a pressure drop inside the pore in accordance with the ideal gas equation of state, resulting in keyhole pore deformation and the occurrence of high-speed microjet. Fig. 4E shows that the speed of the microjet tip increases instantaneously when the condensation in the keyhole pore begins after 4.0 μs. Significant speed difference at the microjet inception portion of the keyhole pore can be observed in Fig. 4E. The maximum velocity occurs in the region near the bottom tip of the newborn keyhole. Specifically, the speed of the microjet tip P_{jet}

increases fourfold from 10.8 m/s to 45.3 m/s in 0.4 μs, and the acceleration reaches 86 m/s², as shown in Fig. 4G. However, the speed increase of Point P_c in the section at $y = 220$ μm is only half of that of Point P_{jet}. The large speed difference between the two points explains their different trajectories, as shown in Fig. 4 (C and D). The trajectory of Point P_{jet} is a straight line before the impinging on a pore boundary which takes only 1.4 μs due to high speed. In contrast, the trajectory of Point P_c is a curve due to its relatively low speed, taking over 3.2 μs before the pore splitting.

3.5.2. Speed difference between P_{jet} and P_c

The pressure drop caused by the vapor condensation in the keyhole pore further amplifies the speed difference between the two points (P_c and P_{jet}), rising from 6.9 m/s to 23.4 m/s. This leads to a more nonuniform velocity distribution around the keyhole pore. Such a highly nonuniform velocity field is precisely the cause for the microjet, especially around the newborn keyhole tip possessing high speed and acceleration. The speed and acceleration can reach 45.3 m/s and 86 m/s², respectively, when the condensation begins. The speed difference
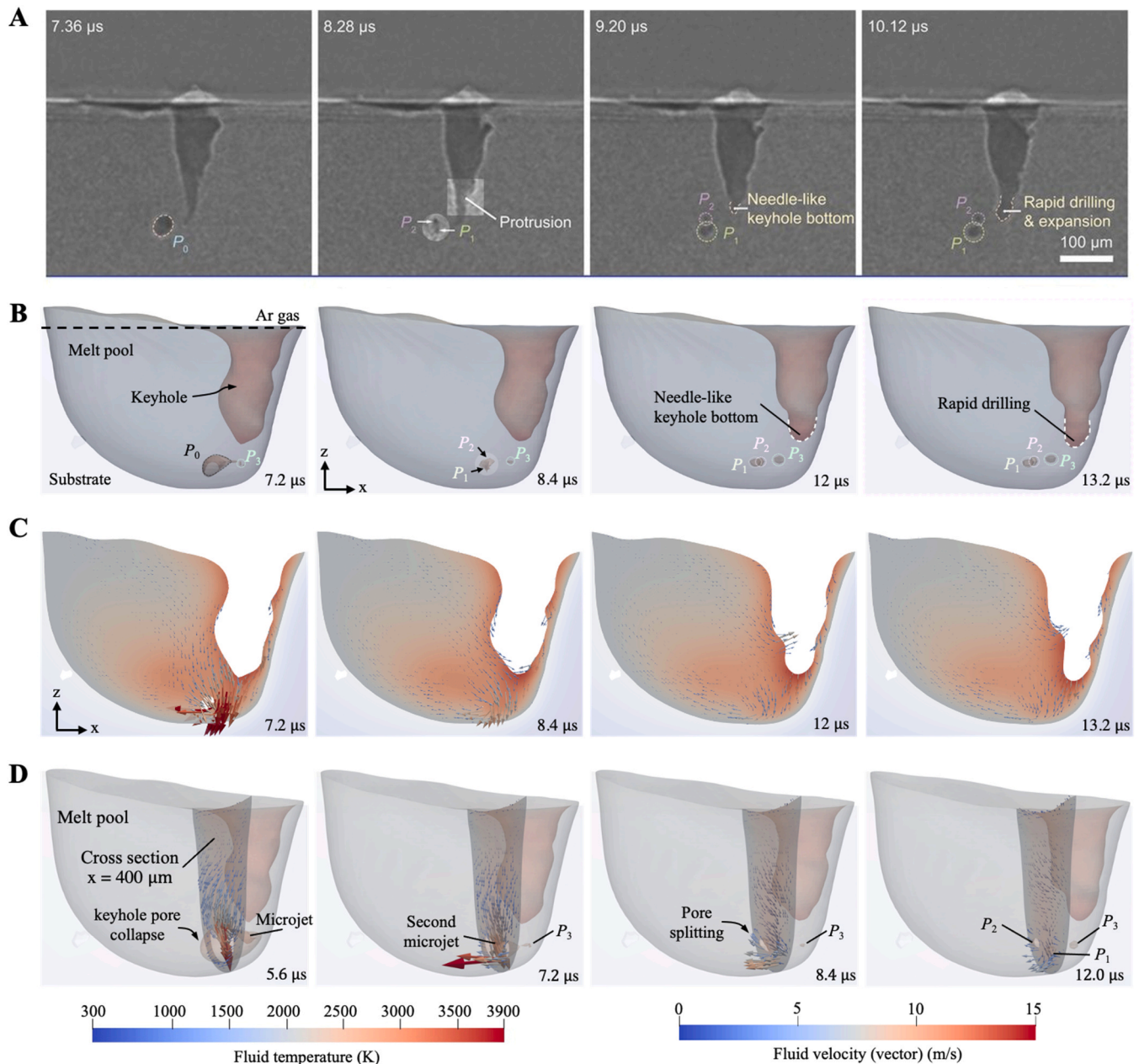
Fig. 6. The splitting dynamics of keyhole pore. (**A**) Megahertz x-ray images of keyhole pore splitting and motion [13]. (**B**) Simulated keyhole pore splitting process in consideration of vapor condensation in the keyhole pore. (**C**) Temperature contour and velocity vector contour of the section at $y = 200$ μm. (**D**) Velocity vector contour in the section at $x = 400$ μm from 5.6 μs to 12.0 μs.

further decreases from 23.4 m/s to 14.9 m/s due to three combined reasons: (1) the increasing surface tension with sharper microjet tip, (2) the slower condensation due to the shrunken surface area of the gas-liquid interface (Fig. 4H), and (3) the collision of the microjet with the bottom wall of the keyhole pore.

3.6. Microjet, newborn keyhole, pore deformation and thermo-mechanical forces

Our high-fidelity three-dimensional numerical simulations also offer unprecedented details that help us uncover new findings to advance our understanding of keyhole pore collapse. Presented in Fig. 5 are results on the dynamics of keyhole pore collapse along the yz-plane against the laser moving direction, extracted from our numerical simulations. It is challenging to obtain these results through other means, such as high-speed x-ray imaging or other techniques.

3.6.1. Velocity distribution and trajectory of microjet

Immediately after the original "J"-like keyhole closure and the condensation in the keyhole pore, the junction connecting the upper newborn keyhole and the keyhole pore undergoes a swift change of flow velocity, which contributes importantly to the generation of microjet. Specifically, as shown in Fig. 5 (A and B), a dramatic increase in pressure and flow velocity is found in this junction region, with a higher increase in the subregion closer to the newborn tip (see also a relevant description in Fig. 4G). At 4.8 μs, the pressure in the shrunken pore is approximately 15 times the pressure in the shrunken pore at 4.0 μs, prior to the onset of vapor condensation. The non-uniform liquid flow pushes the deformation of the keyhole pore transiting from a convex surface to a concave surface observed from the yz-plane, similar to the morphology

change in Fig. 4 (A to D). Consequently, a second microjet emerges and grows in the pore center. It impinges onto the bottom keyhole wall and splits the keyhole pore into two along the laser-moving direction (see 6.0 µs in Fig. 5C and 8.8 µs in Fig. 5D).

3.6.2. Newborn keyhole tip evolutions

The thermal and mechanical forces acting on the newborn keyhole tip, including the recoil pressure, surface tension, and Marangoni's pressure, are further quantified to examine their relative roles played during the above process. The results are presented in Fig. 5E. Notably, the Marangoni's pressure remains smaller than 10 kPa, as such its effect on the newborn keyhole tip is negligibly small. The variations of the recoil pressure and surface tension from 4.0 µs on only show a weak correlation with the velocity of the keyhole tip. Specifically, the rapid acceleration of the keyhole tip accompanied by concurrent keyhole depression leads to a dramatic reduction in the recoil pressure beginning from 4.0 µs. This indicates that the keyhole depression has a prohibiting effect on the keyhole pore collapse, as it helps to enlarge the surface area of the keyhole tip, resulting in a decreased temperature from 4.0 µs to 4.8 µs due to the energy conservation. Meanwhile, continuous laser absorption facilitates the regaining of temperature for the increased surface area from 4.8 µs onwards and hence causes the rebounding of the recoil pressure. The surface tension is mainly dominated by the curvature of the keyhole tip. The keyhole tip becomes sharper from 4.0 µs to 5.6 µs due to rapid keyhole depression, resulting in a steadily increasing surface tension during this stage. However, after 5.6 µs, the strengthened recoil pressure causes a significant expansion of the keyhole tip and a decrease in its curvature, which accounts for the decreasing in surface tension.

3.6.3. Thermo-mechanical forces

Indeed, the overall collapsing process of the keyhole pore is closely correlated with the evolution and relative dominance of the thermosmechanical forces acting on the newborn keyhole tip according to the following three stages. (1) The pressure drop caused by vapor condensation in the keyhole pore first leads to the rapid depression of the newborn keyhole tip and the keyhole pore collapse, causing further drawdown of the recoil pressure and increase of the surface tension acting on the keyhole tip (e.g., before 5.6 µs). (2) A chain of multiple interconnected physical processes, including the rise of surface tension and the drop of the recoil pressure at the keyhole tip, as well as a decelerated condensation rate in the keyhole pore, hinders the collapse of the keyhole pore and reduces the speed of the keyhole tip and the microjet. (3) After the microjet impinges on the bottom wall of the keyhole pore at 6.0 µs, the recoil pressure and the surface tension gradually return to the values when the pore collapse begins due to the slower keyhole depression. The gradual return of the recoil pressure and surface tension further helps to accelerate the keyhole pore-collapse process. Nevertheless, the recoil pressure remains small, with a magnitude at 6.8 µs being only half of that at 4.0 µs, and plays a less role in this stage.

3.6.4. Deformation of keyhole pore

In addition to the microjet on the top-right edge of the keyhole pore, the liquid flow surrounding the keyhole pore can also affect its deformation during the collapse process. For example, the top-right edge suffers a high-speed microjet, while the bottom of the keyhole pore remains largely unperturbed before the impinging of the microjet on the pore bottom. Fig. 3D and Fig. 4 have shown that the pore deformation is only affected by the surface tension and the pressure drop caused by vapor condensation, with the pressure drop being the dominant factor. Fig. 5G further presents a comparison of the changes of five typical velocities at the front, top, side, bottom, and back of the keyhole pore, as illustrated in Fig. 5F.

3.6.5. Flow dynamics surrounding keyhole pore

Five time instances are chosen in presenting Fig. 5G. (1) t_0 refers to the instance when the keyhole pore is going to close. At this time, the front speed of the pore is around 10 m/s, driven by the recoil pressure shown in Fig. 5E. The speed at the top, side, bottom, and back of the pore is smaller than 3 m/s, without an apparent effect of the recoil pressure. (2) At t_1, the speed at the front, top, and back of the keyhole pore increases rapidly due to the vapor condensation in the closed keyhole pore. The speeds at the front and back are only one-fourth or less of that at the front because of the low initial velocity at the top and back, as explained in Fig. 5G. The bottom and side speeds remain stable due to the large drag force from the mushy zone [17]. (3) At t_2, the microjet is going to collide with the bottom wall of the keyhole pore, leading to a dramatic reduction in the front speed from t_1 to t_2. The great front speed further accelerates the top speed and back speed from t_1 to t_2 through the viscous drag force [94], as shown in Fig. 4E. (4) At t_3, the condensation rate is only one-third of its value at t_1 and half of that at t_2 due to the collapsed keyhole pore and decreased contact surface area. The gradually decreasing condensation rate leads to the reduction in the speeds at the front, top, and back of the keyhole pore from t_2 to t_3. In contrast, the bottom speed and side speed rise slowly from t_2 to t_3 due to viscous drag forces by the relatively high front speed. The shrinking keyhole pore further strengthens the connection among the front, bottom, and side of the keyhole pore, enhancing the effect of high front speed on the bottom and side. (5) At t_4, the collapsed keyhole pore begins to split through its center in the *yz*-plane, as shown in Fig. 5 (B to D). The five study points become closer with the shrinking of keyhole pore, and the differences between the front speed, top speed, side speed, and bottom speed reduce rapidly from t_3 to t_4. Note that, the bottom speed is close to 0 m/s as its direction is opposite to that of the front speed.

3.7. Splitting of keyhole pore

Fig. 6A shows an experimental observation of the splitting process of a keyhole pore [13], where the formation mechanism is attributed to the impinging of a high-speed microjet on the opposite wall of the pore. To further validate the proposed numerical model and examine how vapor condensation dictates the splitting of a keyhole pore, we present in Fig. 6 (B to D) the simulated keyhole pore splitting and the corresponding velocity field. Fig. 6B (7.2 µs and 8.4 µs) shows that two splitting processes, driven by two high-speed microjets with different directions, generate three pores (P_1 to P_3).

3.7.1. First splitting

The first splitting caused by the first microjet (Fig. 4C and E) occurs in the region close to the keyhole bottom. It separates the initial keyhole pore into two child pores P_0 and P_3. The shape of P_3 at 7.2 µs resembles a spike (see Fig. 6D, time 7.2 µs) since it derives from a narrow gap between the microjet and the keyhole pore, as shown in Fig. 4D and Fig. 5C. Pore P_3 gradually becomes more spherical from 7.2 µs to 12 µs due to surface tension. The merging of Pore P_3 with other small pores results in its volume expansion and an increase in the equivalent pore size. (around 5.8 µm from 7.2 µs to 11.2 µs), as shown in Fig. 4F. However, this phenomenon was not observed in the experiment [13] since the bottom walls of the microjet and keyhole pore are overlapped entirely, as shown in Fig. 4D. It appears that a larger initial keyhole pore expands the pore gap caused by the collision of the microjet and keyhole pore, increasing the potential for the pore formation.

3.7.2. Second splitting

The second splitting occurs approximately at the center of Pore P_0 in the *yz*-plane as a result of the second microjet in the *z*-direction, as shown in Fig. 5D and Fig. 6D (7.2 µs). The maximum speed of this second microjet is only one-third of that of the first one, leading to a longer duration (from 4.8 µs to 8.0 µs) to form the concave surface in Pore P_0, as presented in Fig. 5D. The impinging of the second microjet on the
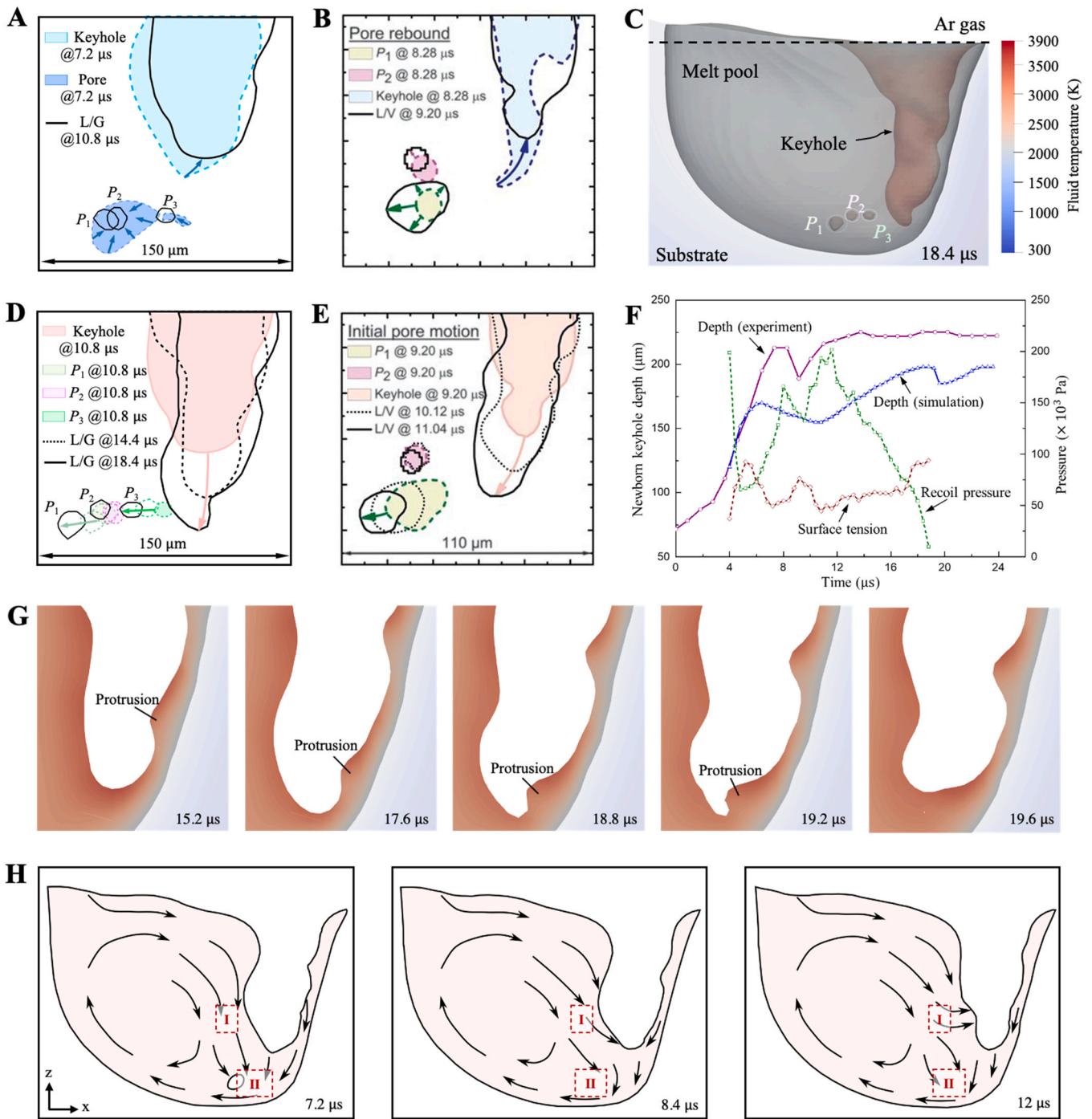
Fig. 7. Rebound and drilling dynamics of the newborn keyhole. (**A** and **B**) Rebound of the newborn keyhole by our simulation (A) and observed from experimental results (B) [13]. (**C**) Simulation results with the melt pool, keyhole and three pores at 18.4 μs. (**D** and **E**) Drilling of the newborn keyhole and pore motion in simulation results (D) and experimental results (E) [13]. (**F**) Comparison of the newborn keyhole depth between the simulation results and experimental results [13], and the recoil pressure and surface tension at the newborn keyhole tip. (**G**) Section profile of the keyhole with the temperature contour at $y = 200$ μm. (**H**) Schematic of the liquid flow in the melt pool based on Fig. 6C.

bottom wall of Pore P_0 at 8.4 μs further generates two split pores (Fig. 4 F), P_1 and P_2. Note that, asymmetric pore splitting may lead to two pores with significantly different sizes, such as the two pores P_1 and P_2 observed in the experiment (Fig. 6A). The equivalent pore sizes of P_1 and P_2 obtained from 2D information (Fig. 4C) in experimental observations and simulation results both fluctuate after the pore splitting. This fluctuation is induced by multiple factors, such as surface tension, pore shape, continuing vapor condensation, and acoustic waves [95,96]. Further improvements in the evaporation model and condensation

model may help to quantitatively capture the evolutions of pore size and relevant mechanisms. The first microjet also plays an important role in the second splitting process. First, with the decreasing volume of Pore P_0, the first microjet helps to increase the speed of the second microjet through the viscous drag force (see Fig. 5G). Second, the high front speed derived from the first microjet, in conjunction with the top and back speeds as shown in Fig. 5 (F and G), further compresses the center of pore P_0 in causing the second splitting.
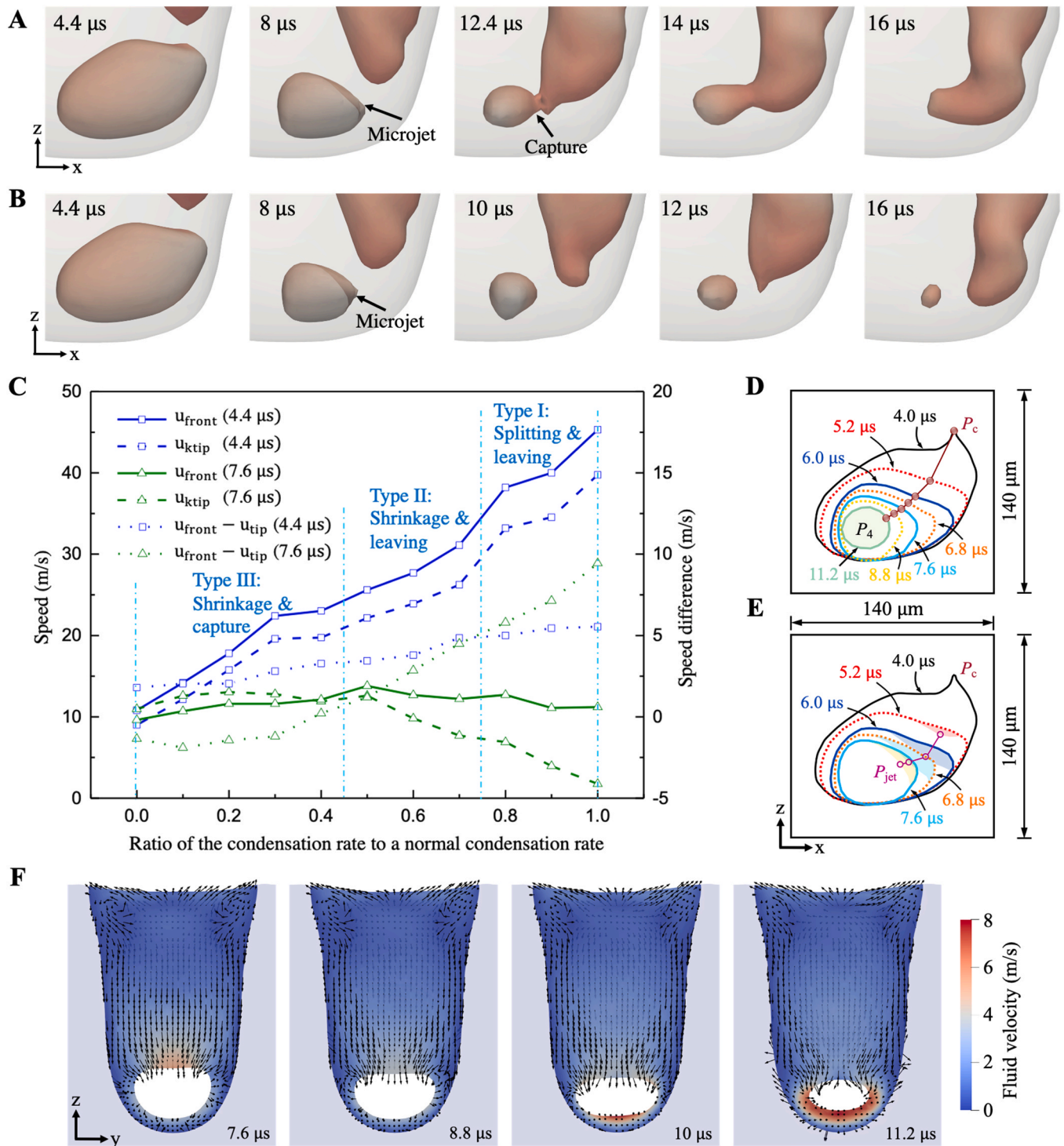
Fig. 8. Simulation of the keyhole pore with different condensation rates. (A and B) Simulated keyhole pore evolutions with 0.4 (A) and 0.5 (B) times of the standard condensation rate. (C) Comparison of speeds at the front of the keyhole pore (u_{front}) shown in Fig. 5E and the keyhole tip (u_{ktip}), and the corresponding speed difference ($u_{front} - u_{ktip}$) at 4.4 μs and 7.6 μs with different condensation rates. (D and E) Contours of the pore (D) and microjet (E) morphologies with a half of the standard condensation ratio. (F) Velocity vector contour in the section at $x = 395$ μm, with a half of the standard condensation ratio. The section at $x = 395$ μm passes through pore P_4 generated at 11.2 μs.

3.7.3. Conditions for the first microjet formation

From our numerical results, we summarize that the formation of microjet at a point P on the liquid-gas interphase may need to satisfy three requirements. (1) Both the velocity and velocity gradient at point P are significantly larger than in other locations at the liquid-gas interphase, e.g., a maximum velocity and gradient at 45.3 m/s and $1.39 \times$ 10^6 s^{-1} for the first microjet (Fig. 4E and Figs. 5B), and 10.2 m/s and 1.75×10^5 s^{-1} for the second microjet (Fig. 6D); (2) The width and length of the region with a significant velocity gradient should be smaller than that of the keyhole pore; (3) The initial velocity direction at the point P aligns approximately perpendicular to the liquid-gas interphase. Due to the Gaussian distributed laser energy, the velocity peak

occurs near the central section of the melt pool along the laser moving direction. A microjet that matches three requirements would first exist in the region between the keyhole pore and keyhole bottom due to the recoil pressure acting on the keyhole bottom and the vapor condensation in the keyhole pore, as shown in Fig. 4E and Fig. 5B.

3.7.4. Conditions for the second microjet formation

Another microjet (Fig. 6D) occurs at the keyhole pore top after the collision of the first microjet and keyhole pore bottom for two reasons. (1) Though the velocity at the keyhole pore front or bottom is larger than at the keyhole pore top (Fig. 5G), the velocity direction does not satisfy the third requirement. (2) The liquid at the keyhole pore top is driven by a more significant viscous drag force induced by the first microjet than the back of the keyhole pore. Since the second microjet splits pore P_0 into two tiny pores from the central section of the melt pool and only limited vapor condensation occurs in the two tiny pores, there are no more microjets that satisfy all three requirements.

3.8. Keyhole rebound and drilling

A new keyhole can be generated after the collision of keyhole walls and the keyhole pore closure. Presented in Fig. 7 is an example from our simulation of the keyhole-reshaping process and the corresponding recoil pressure and surface tension at the keyhole tip. The instability of the newborn keyhole is caused by multiple physical mechanisms, including the keyhole protrusions, multiple laser reflections, and surrounding liquid flow.

3.8.1. Comparison with experimental observations

Zhao [13] argued that the keyhole rebound is caused by the protrusion structure at the keyhole bottom, the acoustic wave induced by the pore rebound and the surface tension effect, and the focus of the laser intensity causes the keyhole drilling through multiple reflections. The protrusion structure indeed causes the reduction of the recoil pressure applied to the keyhole tip since it decreases the absorption of reflected rays by the keyhole bottom tip. Our simulation results shown in Fig. 7 (F and G), from 8.0 μs to 9.6 μs and 15.2 μs to 19.2 μs, confirm the same trend of the recoil pressure. The increase of recoil pressure from 9.6 μs to 11.6 μs also confirms the speculated mechanism of the keyhole drilling. A diverging argument from our numerical simulation is the role played by the acoustic wave induced by the pore rebound. The pore rebound can indeed be a result of the pore reshaping caused by the liquid flow and surface tension and the merging of surrounding tiny pores, such as the pores P_1 and P_3 shown in Fig. 7 (A and D). However, our simulation results (Fig. 7) indicate that the rapidly decreased recoil pressure and increased surface tension, in conjunction with the adjusted liquid vortex in the melt pool, play a key role in affecting the keyhole reshaping and hence keyhole drilling.

3.8.2. Keyhole fluctuations

Three stages can be identified based on the depth change of the newborn keyhole (Fig. 7F) to explain the instability at the keyhole tip and the corresponding physical mechanisms.

From 4.0 μs to 6.4 μs, dramatic drilling occurs due to the pressure drop induced by the vapor condensation in the keyhole pore. This sudden increase of the keyhole depth causes a decrease in the surface temperature and hence curvature radius of the keyhole tip. This further induces a rapid reduction of the recoil pressure and an increase of the surface tension, as explained in Fig. 5E.

From 6.4 μs to 10.8 μs. There are two contributing factors to the keyhole rebound. First, the velocity drop of the microjet or the front speed of the keyhole pore in Region II (Fig. 7H) weakens the vortex strength, leading to a velocity change in Region I from the *z*-direction to a direction inclined to the *z*-direction. The fluid with an inclined velocity in Region I (Fig. 7H, 8.4 μs) fills the keyhole bottom, causing the keyhole rebound. Second, the small recoil pressure at 6.4 μs cannot sufficiently

resist the keyhole rebound, and the equivalent pressure induced by the surface tension is at a comparable magnitude with the recoil pressure at 6.4 μs. This leads to the acceleration of the keyhole rebound until the recoil pressure gradually gains strength due to the continuing laser energy input.

From 10.8 μs to 18.8 μs, the fluid in Region I gradually flows along the x-direction, causing the formation of a needle-like keyhole bottom. The combination of the concentrated laser energy in the needle-like keyhole bottom and the strengthened recoil pressure at the end of the second stage leads to rapid keyhole drilling.

3.8.3. Relevant conclusions

Three conclusive observations can be drawn from Fig. 7F. (1) The drilling caused by the pressure drop in the keyhole pore due to vapor condensation can reach 3.6 times faster than that caused by the recoil pressure and the concentrated laser energy in the keyhole. (2) The evolution of the recoil pressure is almost negatively correlated with to that of the surface tension. For example, the protrusion structure induces a decreased recoil pressure by affecting the reflected rays absorbed by the keyhole bottom and meanwhile leads to the generation of a sharper keyhole tip with a larger surface tension, as shown in Fig. 7G. (3) The vortex induced by the vapor condensation enhances the keyhole instability by causing keyhole drilling and rebound, and the formation of needle-like keyhole bottom. The protrusion structure also causes a higher keyhole instability by generating a sharp keyhole tip and changing the direction of reflected rays, which can further compound the vortex's effect, as shown in Fig. 7F (6.4 μs to 10.8 μs).

3.9. Condensation rate

As has been emphasized, the vapor condensation in the keyhole pore plays a crucial role in the pore-collapse process (Fig. 4 and Fig. 5), pore splitting (Fig. 6), and the keyhole fluctuations (Fig. 7). According to Eq. (6), the condensation rate varies with the material type and the temperature field dominated by the input laser energy. In this section, ten comparison cases (Fig. 8) with a condensation rate ranging from 0 to 0.9 times the standard condensation rate are further considered to study the effect of the condensation rate on the keyhole pore deformation and motion. The standard condensation rate is calculated by Eq. (6) in the "*Multi-way phase transitions*" section. The product of the condensation rate and the condensation duration remains constant. The numerical settings are identical with preceding sections, except for the condensation rate and duration.

3.9.1. Three types of keyhole pore deformation and motion

It is evident from Fig. 8 that the pressure drop rate in the closed keyhole pore is reduced with a decreasing condensation rate. It leads to an approximately linear decline in both the initial pore-collapse speed and the difference between the pore-collapse speed and the keyhole drilling speed at 4.4 μs (Fig. 8C). The decreasing initial pore-collapse speed further leads to three distinct types of keyhole pore deformation and motion, including the "splitting and leaving" (Type I, Fig. 6), "shrinkage and leaving" (Type II, Fig. 8B), and "shrinkage and capture" (Type III, Fig. 8A). Fig. 8C further shows the corresponding region of the condensation rate that Types I to III belong to. There are two significant aspects to explain the formation of three types of keyhole pore deformation and motion.

First, rather different physical phenomena can be observed in Types II and III. (1) The reducing pore-collapse speed caused by the decreasing condensation rate leads to a weaker microjet (Fig. 8C). The weak microjet shown in Fig. 8 (A, B, and E) disappears entirely before it possibly impinges on the bottom wall of the keyhole pore, which means that the first splitting, as observed in Fig. 6, does not occur. (2) The trajectory of Point P_{jet} shows as a curve (Fig. 8D) in this case rather than a straight line (Fig. 4D) as in the normal condensation rate case. The curvature of the trajectory of Point P_c also decreases, representing a
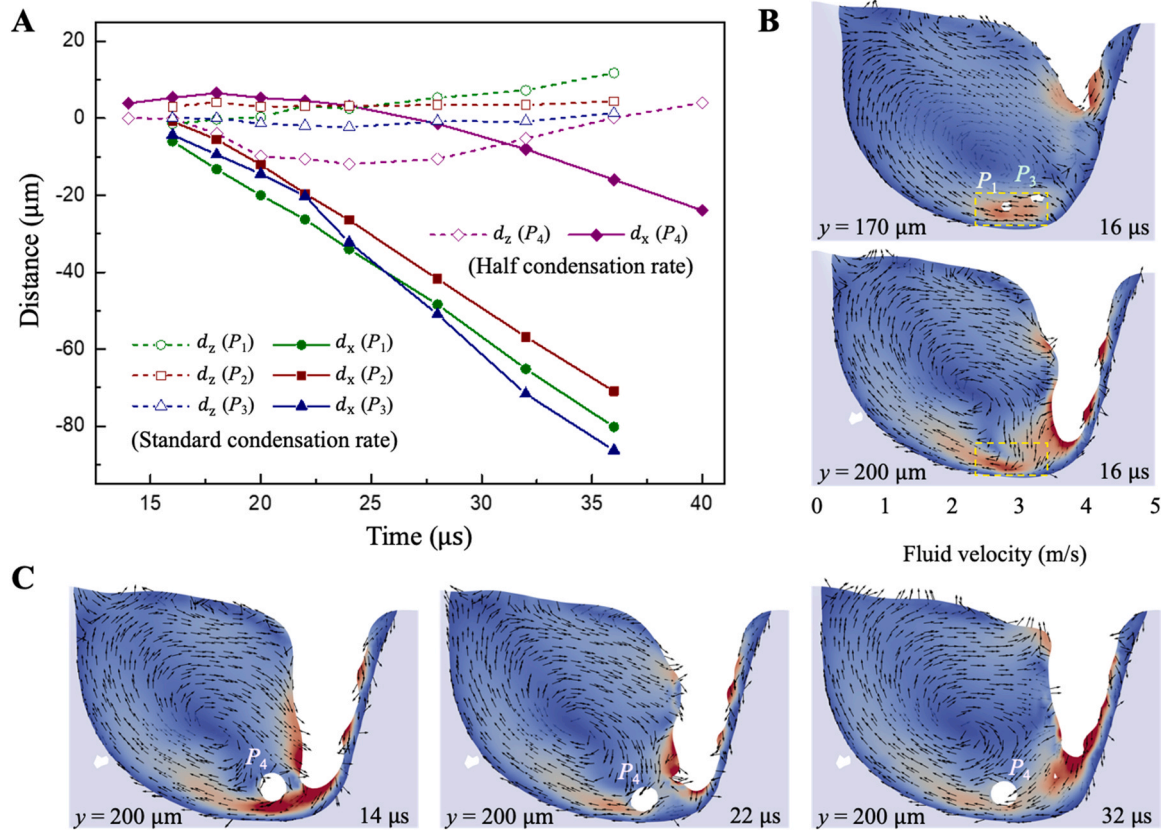
Fig. 9. Comparison of the pore motion between simulation results with two different condensation rates. (A) The moving distance of four pores in the x-z plane. The pore position at 16.0 μs is selected as the reference position for the case with a standard condensation ratio, and the pore position at 14.0 μs is selected as the reference position for the case with a half condensation ratio. A positive d_z means that the pore moves upward, and a positive d_x means that the pore moves to the keyhole. The distance in the y-direction d_y is ignored here due to its relatively small value compared with d_x and d_z. (B) Contours of velocity vector of the two cross sections at $y = 170$ μm and $y = 200$ μm at 16.0 μs. (C) Velocity vector contour of the section at y = 200 μm at 14.0 μs, 22.0 μs and 32.0 μs.

stable collapse process. (3) A second microjet cannot be observed in Fig. 8F. The liquid flow at the top of the keyhole pore squashes the keyhole pore instead of forming a second microjet inside the pore to cause the pore splitting.

Second, the speed difference ($u_{front} - u_{ktip}$) at 7.6 μs in Fig. 8C indicates rather different keyhole pore motions. In Type III, the speed difference is negative or close to zero, which means that the keyhole drilling speed is larger than or similar to the keyhole shrinkage speed. With continuous laser illumination, the keyhole tip driven by the increasing recoil pressure further captures the shrinking keyhole pore, as shown in Fig. 8A. In Types I and II, the pore-collapse or pore-shrink speed is faster than that of the keyhole drilling, increasing the difficulty to capture the keyhole pore. Moreover, the higher speed at the keyhole tip induced by the stronger vapor condensation in the keyhole pore may result in a rapid reduction in the temperature and recoil pressure at the keyhole tip, as shown in Fig. 5B. Therefore, the keyhole pore in Types I and II moves away from the keyhole. The mechanisms of further pore motion in Types I and II will be discussed in the next section.

3.9.2. Relevant conclusions

Therefore, the vapor condensation in the keyhole pore does dominate its collapse, splitting, and motion process, including the generation of two microjets and the velocity field of the surrounding liquid and the keyhole tip. A decreasing condensation rate helps to improve the stability of the keyhole and keyhole pore by forming a more uniform velocity distribution with a lower peak speed around the pore. This effect is particularly significant in the region between the pore and keyhole bottom. Our simulation results show that controlling the vapor

condensation appears to be a feasible strategy to possibly reduce the porosity in L-PBF. It is recommended to adopt a condensation rate in Type III (Fig. 8C) to eliminate the pore induced by the "J"-like keyhole.

3.9.3. Practical optimization strategy

Although a few approaches, such as surface coating and ion implantation, have been proposed to affect the condensation rate of vapor at metallic surfaces [97,98], it remains a challenge to adopt these methods or develop new ones to accurately control the condensation rate during the L-PBF process. A feasible method currently employed involves the use of a high-speed shielding gas flow (e.g., 4 m/s [99]) to remove the vapor plume [100–103], which decreases the vapor content in the keyhole and reduces vapor condensation in the keyhole pore. Studies have shown that the shielding gas flow can lead to a more stable melt pool [104,105] and significantly reduce the porosity of produced parts [99, 106–109]. In conjunction with the shielding gas flow, adaptive laser power can be used to diminish evaporation in the keyhole by reducing the laser power before keyhole pore formation. Recently, two adaptive laser power strategies [36,45] have been proposed to address porosity caused by the deep keyhole at the starting turning points of the laser scanning path. However, unlike these two specific points of the scanning path, accurate prediction of keyhole pore formation is essential for the application of adaptive laser power during a complete scanning path. The adaptive laser power strategy and the prediction strategy of the keyhole pore formation will be subject to further study in the future.

3.10. Keyhole pore motion

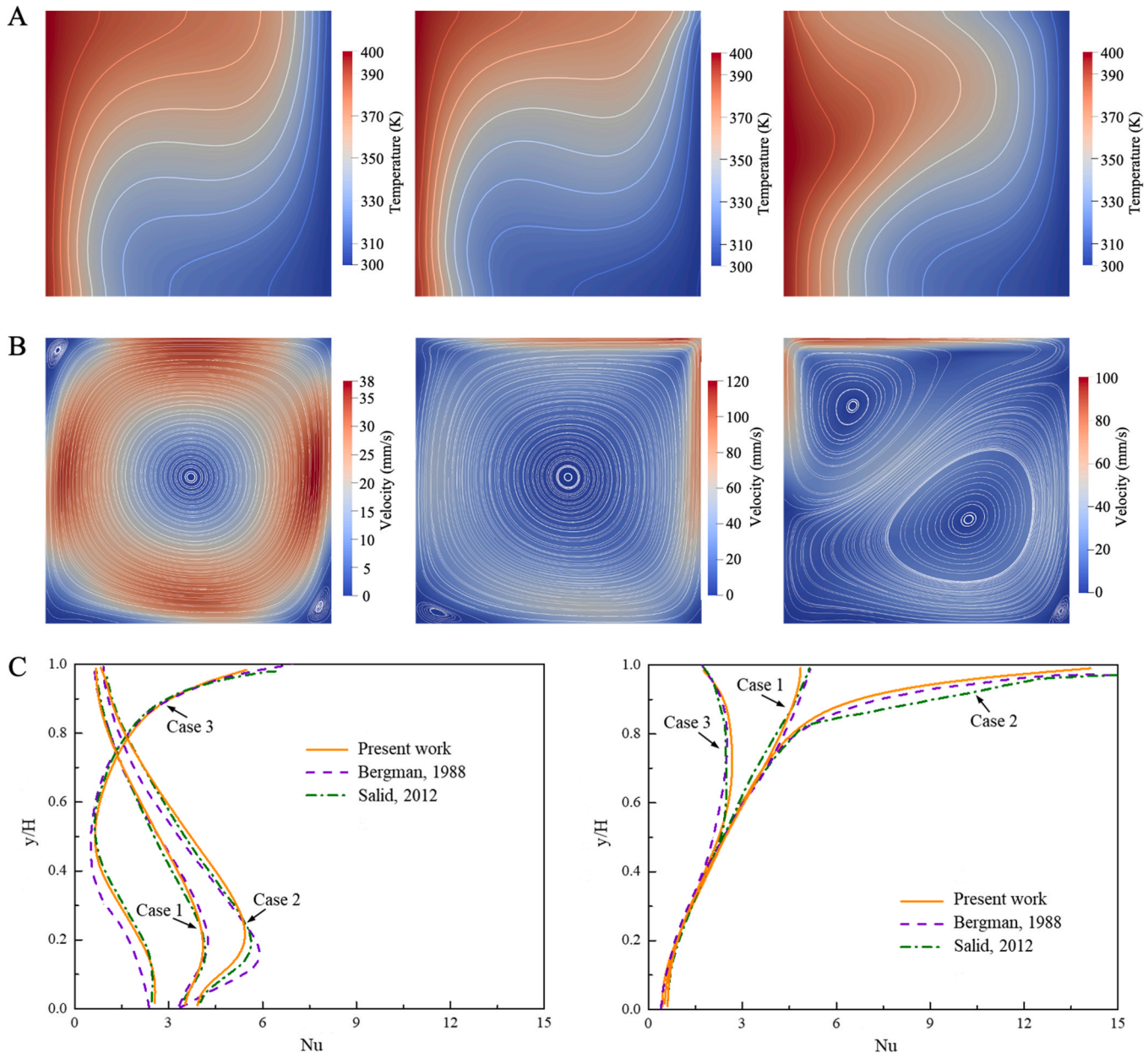The two pores P_1 and P_2 observed in the experiment [13] (Fig. 6A)

Fig. A.1. . Benchmark case I: single-phase Marangoni driven flows. (**A**) Isotherms of cases 1 (left), 2 (middle), and 3 (right). (**B**) Streamlines of cases 1 (left), 2 (middle), and 3 (right). (**C**) Comparison of local Nusselt number distributions at the hot (left) and cold (right) walls [74,111]. Details of three cases, such as the model setup, can be found in the literature [74].

underwent different motions in the melt pool. The larger Pore P_1 was directly pushed away from the keyhole bottom, while the smaller Pore P_2 above Pore P_1 fluctuated around the keyhole bottom. It was speculated [13] that the needle-like keyhole bottom may emit a strong acoustic wave and cause a liquid jet [94], driving Pore P_1 to migrate away, with facilitation by the thermocapillary force [110] and the viscous drag force [94]. However, the kinetic energy from the acoustic wave might not be sufficient to push Pore P_2, which is further controlled by the competition between the thermocapillary and viscous drag forces. Rather, phase explosion was supposed [13] to contribute to its observed motion. The experimental study also attempted to connect the pore motion with other physical phenomena, such as the keyhole rebound and drilling. It is instructive to revisit the mechanism of pore motion based on our numerical results. To examine how the melt flow dictates the pore motion, we present in Fig. 9 the contours of the velocity vector and the moving distance of the four pores in the two simulation cases

with different condensation ratios. The following study shows that the pore motion is highly dependent on the initial pore position and is closely related to the keyhole fluctuations.

3.10.1. Different pore motions

Fig. 9A shows that three pores P_1, P_2, and P_3, generated in the case with a standard condensation rate, show a similar trend of motion, continuously moving away along the melt pool boundary. Due to the approximately symmetric pore splitting induced by the second microjet shown in Fig. 5C and Fig. 6D, P_1, P_2, and P_3 are formed near the side of the melt pool along the y-direction, e.g., the section at 170 μm. In contrast, Pore P_4, generated in the case with a half condensation rate, is formed in the center of the melt pool and undergoes a complicated motion featured by three stages: (1) It moves closer to the keyhole before going downwards from 14 μs to 18 μs; (2) It then moves away from the keyhole and keeps moving downward from 18 μs to 24 μs; (3) It moves
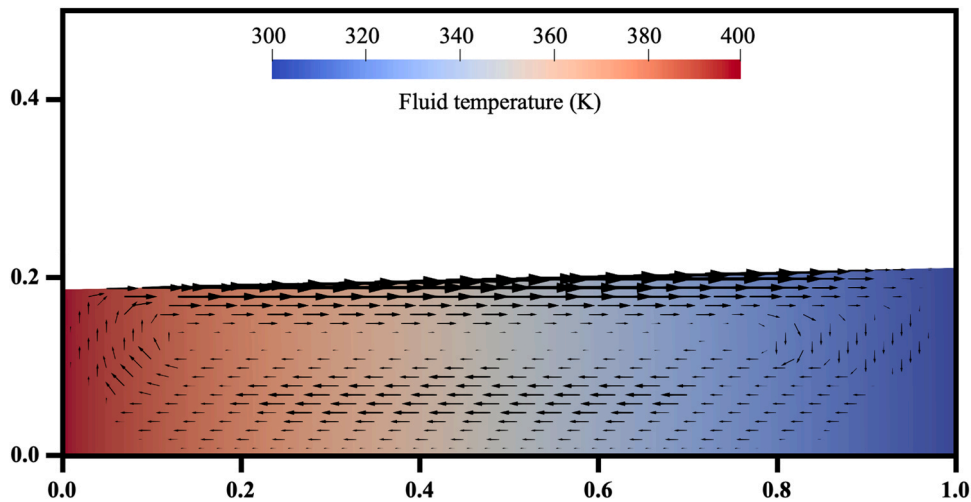
Fig. A.2. . Benchmark case II: two-phase Marangoni driven flows with contours of velocity vector and temperature field at steady state. The introduction and model setup of this case can be found in the literature [74].
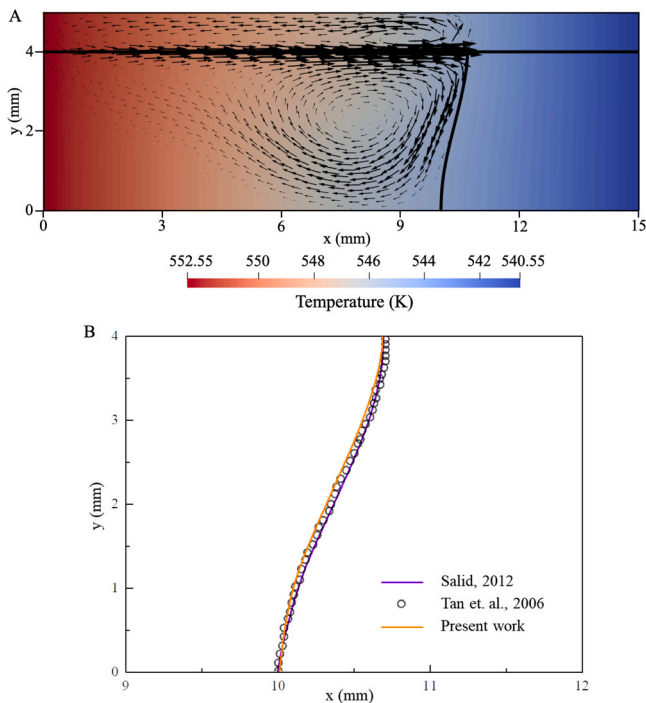

Fig. A.3. . Benchmark case III: free surface Marangoni-driven flows with phase change. (**A**) Contours of fluid velocity vector and fluid temperature field at steady state. (**B**) Comparison of the shape of liquid-solid interface at steady state [74,115]. The introduction and model setup of this case can be found in the literature [74].

upwards and continues to leave the keyhole from 24 μs to 40 μs.

3.10.2. Effect of initial pore position

Fig. 9B shows that the liquid vortex in the melt pool varies in different cross sections, which may be a primary reason accounting for the observed difference in the pore motion. For example, Fig. 9B compares the velocity vector contours of two cross sections in the xz-plane at 16 μs. The first section at $y = 170$ μm is close to the sideway of the melt pool, and the second section at $y = 200$ μm is the central section of the melt pool. The velocity of the region highlighted by the yellow dotted block in the first section is stable and uniform, continuously driving pores P_1 and P_3 along the negative x-direction. However, in the second

cross section, the velocity direction and magnitude vary significantly with the position in the highlighted region. The velocity direction changes from the negative z-direction to the negative x-direction, and the liquid at the bottom has the largest velocity. Similarly, the intricate velocity distribution in the central section causes the complicated motion of pore P_4 (Fig. 9C). First, the liquid above pore P_4 with a velocity inclined to the keyhole tip drags pore P_4 to the keyhole tip. The bottom liquid with the high speed dominates the motion of Pore P_4 and carries P_4 away to move from the keyhole. Third, Pore P_4 moves within the vortex along the melt pool boundary.

3.10.3. Effect of keyhole fluctuations

Fig. 9C further shows that the vortex in the melt pool is also affected by the keyhole fluctuations, such as the keyhole rebound and drilling. Note that, there is no vapor condensation during the pore-motion process (after 14 μs). The recoil pressure acting on the keyhole bottom is the original driving force for the liquid vortex that generates high-speed liquid flow in the keyhole bottom. While the surface tension helps to resist the keyhole drilling, the protrusions in the front keyhole wall act to decrease the laser absorption in the keyhole bottom. They work together to cause a slowing down of the fluid flow in the keyhole bottom. The evolutions of the recoil pressure and surface tension in conjunction with keyhole morphological changes, e.g., the needle-like keyhole and protrusions, cause the keyhole rebound and drilling. A typical example can be found in Fig. 7F. The keyhole rebound at 32 μs shown in Fig. 9C drives Pore P_4 to migrate away since it generates a wide liquid flow region with a relatively uniform velocity field in the melt pool bottom, similar to the section at $y = 170$ μm shown in Fig. 9B. In contrast, the rapid keyhole drilling at 14 μs shown in Fig. 9C dramatically causes the velocity increase in a narrow region in the melt pool bottom. Though the maximum velocity in the melt pool bottom at 14 μs is around twice the magnitude of that at 32 μs, it only affects the bottom tip of pore P_4 and finally leads to pore fluctuation.

4. Conclusions

We employ a highly-fidelity computational approach recently developed [50] to examine the instability mechanisms of a moving keyhole and keyhole pore observed in metal additive manufacturing. The numerical tool fully considers critical interdependent physics of heat transfers, multi-way phase transitions, and thermo-mechanical dynamics during a typical laser melting process. It helps to offer 3D, high-resolution simulations of the laser melting process and overcome the constraint of experimental testing means, such as high-speed X-ray
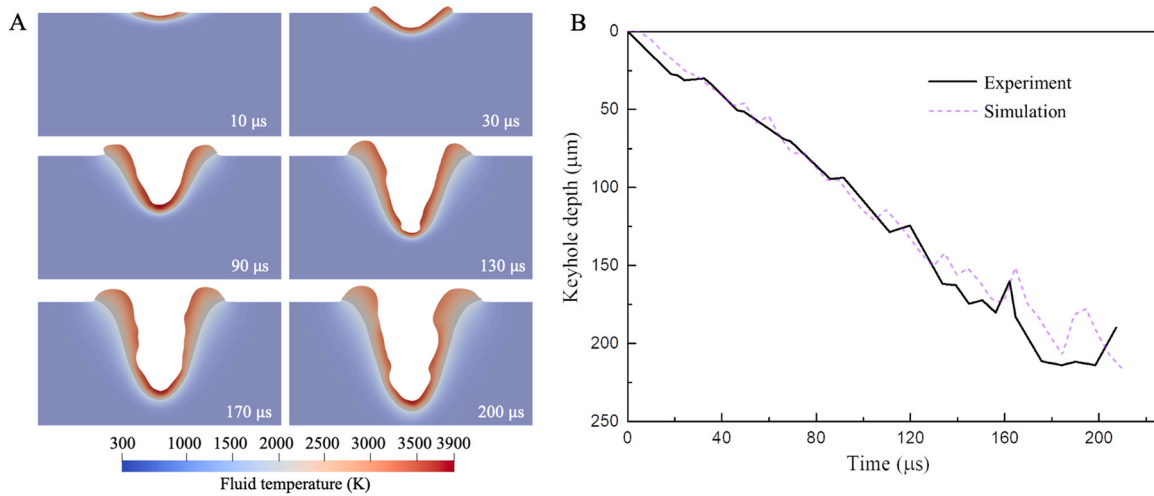
Fig. A.4. . Benchmark case IV: keyhole evolutions with a stationary laser beam. (**A**) Central cross-section profile of the simulated keyhole in terms of temperature contour. (**B**) Comparison of the keyhole depth between simulation and experimental results [18]. The laser diameter is 140 μm and the laser power is 364 W. The model setup has been introduced in Section 3.1.

Table A.1
Benchmark case II: comparison of free surface heights (dimensionless) at left and right walls.

Authors	Dimensionless free surface heights	
	Left wall	Right wall
Sasmal and Hochstein (1994)[112], simulation	0.174	0.224
Francois et al. (2006)[113], simulation	0.187	0.209
Saldi (2012)[74], simulation	0.187	0.208
Present, simulation	0.1884	0.2122
Sen and Davis (1982)[114], analytical	0.188	0.213

Table A.2
Physical parameters of Ti-6Al-4 V [17,50] and ambient gas [17,50] adopted for the simulations.

Parameter	Value and units	Parameter	Value and units
Room temperature	$T_0 = 300\text{K}$	Solidus temperature	$T_s = 1878\text{K}$
Liquidus temperature	$T_l = 1923\text{K}$	Boiling temperature	$T_{LV} = 3133\text{K}$
Molar mass	$M = 446.07\text{g/mol}$	Convective heat transfer coefficient	$h = 19\text{kg} \bullet \text{s}^3\text{K}$
Viscosity of liquid Ti-6Al-4 V alloy	$\mu_l = 0.005\text{Pa·s}$	Viscosity of solid Ti-6Al-4 V alloy	$\mu_l = 1.13\text{Pa·s}$
Latent heat of fusion	$L_f = 2.88 \times 10^5 \ \text{m}^2/\text{s}^2$	Permeability coefficient	$K_c = 5.56 \times 10^6 \ \text{kg/(m}^3\text{s)}$
Latent heat of evaporation	$L_V = 9.7 \times 10^6 \text{m}^2/\text{s}^2$	Constant to avoid division by zero	$C_k = 10^{-5}$
Surface tension coefficient at melt point	$\sigma_l = 1.68\text{kg/s}^2$	Change rate of surface tension coefficient	$\frac{\partial \sigma}{\partial T} = -2.6 \times 10^{-4} \ \text{kg/(s}^2\text{K)}$
Refractive index [77]	$e = 3.47$	Coefficient related to the electrical conductance[44]	$\varepsilon = 0.2$
Reflectivity at room temperature [66]	$f_{R0} = 0.95$	Reflectivity at liquidus temperature [66]	$f_{Rl} = 0.63$
Absorption coefficient at room temperature [13]	$\gamma_0 = 47.1 \ \mu\text{m}^{-1}$	Absorption coefficient at liquidus temperature[50,52,67,70]	$\gamma_0 = 0.192 \ \mu\text{m}^{-1}$
Gas density	$\rho_2 = 1.87\text{kg/m}^3$	Viscosity of gas	$\mu_2 = 2.5 \times 10^{-5}\text{Pa·s}$
Heat capacity of gas	$C_2 = 500\text{J/(kg} \bullet \text{K)}$	Thermal conductivity of gas	$k_2 = 0.021 \ \text{W/} (\text{m} \bullet \text{K})$

imaging that provide, which can only provide two-dimensional morphologies of the keyhole and melt pool. The numerical tool faithfully reproduces various aspects of keyhole instability, including its rotation, drilling, rebound, and pore formation, as well as keyhole pore instability, including collapse, splitting, and motion, which have been observed in in-situ experiments. The simulation results are rigorously analyzed to establish connections between these instability patterns and multiple new interconnected physical mechanisms that have not been discussed before. Specifically, the following conclusions can be drawn from this numerical study.

Protrusions in the keyhole wall serve to enhance keyhole fluctuations by accelerating the keyhole neck closure, altering the direction of the reflected rays from the front keyhole wall, causing changes in the bottom morphology of the keyhole, and helping the transportation of high-temperature liquids to the keyhole bottom.

Vapor condensation can play a major role in causing two microjets that induce the collapse and splitting of keyhole pore and rapid keyhole drilling. Our numerical simulations show the first microjet splits the keyhole pore along the keyhole drilling direction, and the second microjet splits the keyhole pore from the pore center in an approximately downward direction. The occurrence of microjet requires a significantly high velocity gradient and a velocity direction aligning perpendicular to the pore surface.

A lower condensation rate helps to weaken the microjet strength to avoid the pore splitting by leading to a more uniform velocity distribution around the keyhole pore. Three types of keyhole pore deformation and motion are identified with a decreasing condensation rate. Pore splitting only occurs in a "splitting and leaving" type, whereas the keyhole pore in a "shrinkage and capture" type will be captured by the keyhole. Adopting the condensation rate in the "shrinkage and capture"

type is recommended to possibly eliminate the keyhole pore in practical laser melting.

Five interconnected factors, including the vapor condensation, liquid vortex, recoil pressure, surface tension, and keyhole morphology, collectively dictate the keyhole fluctuations. The vapor condensation and recoil pressure play a role strengthening the keyhole drilling and liquid vortex, whereas the surface tension shows an opposite effect. The liquid vortex dominates the dynamics of the keyhole rear wall. For the keyhole morphology, a sharp keyhole tip is caused by the keyhole drilling, such as the needle-like keyhole tip. It helps to enhance both the

Table A.3

Temperature-dependent thermal parameters of Ti-6Al-4 V [75] adopted for the simulations.

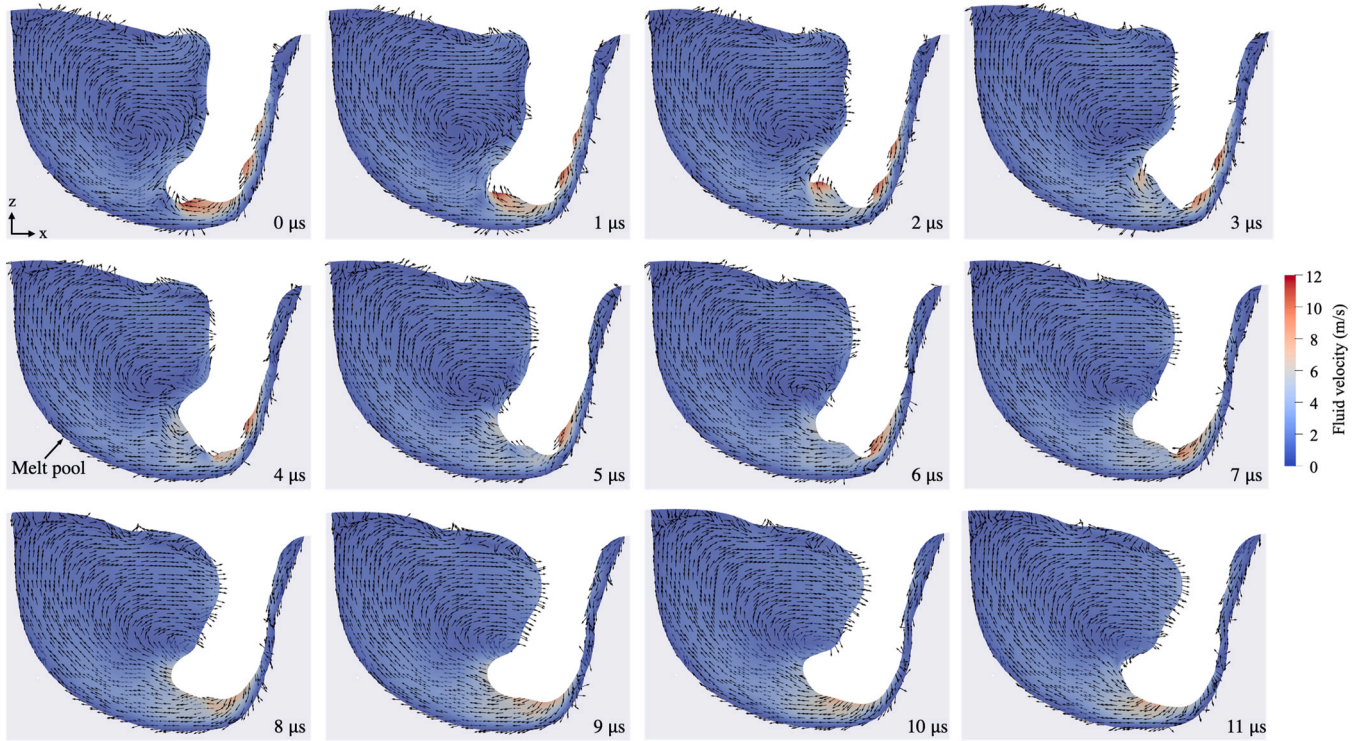| Material	Parameter and units	Value or equation
Ti-6Al-4 V	Density (kg/m^3)	$\rho_1 = \begin{cases} 4420 & T < 1268K \\ 4420 - 0.154(T - 298) & 1268K < T < 1923K \\ 3920 - 0.680(T - 1923) & T \geq 1923K \end{cases}$
	Heat capacity $(J/(kg \bullet K))$	$C_1 = \begin{cases} 411.5 & T < 1268K \\ 411.5 + 0.2T + 5 \times 10^{-7}T^2 & 1268K < T < 1923K \\ 830 & T \geq 1923K \end{cases}$
	Thermal conductivity $(W/(m \bullet K))$	$k_1 = \begin{cases} \& 19.0 & T < 1268K \\ -0.80 + 0.018T - 2 \times 10^{-6}T^2 & 1268K < T < 1923K \\ 33.4 & 1923K < T < 1973K \\ 34.6 & T \geq 1973K \end{cases}$

Fig. A.5. Simulated velocity vector contour of the central cross section at $y = 200$ μm during the formation process of the "J"-like keyhole.

surface tension due to increased curvature and the recoil pressure by concentrating the laser intensity through multiple reflections.

The pore motion is mainly driven by the vortex in the melt pool which is closely related to both the pore position and keyhole fluctuations including keyhole drilling and rebound. The vortex near the melt pool boundary is more stable and uniform than in the melt pool center. A rapid keyhole drilling can significantly increase the velocity of a narrow region in the melt pool bottom, amplifying the instability of the vortex. On the other hand, the keyhole rebound can serve to stabilize the liquid vortex by generating a wider region with a relatively uniform velocity distribution.

This study constitutes a first step towards understanding the micro-mechanisms of keyhole pore evolutions in L-PBF and developing possible optimization strategies for keyhole pores, based on a rigorous, physically based computational approach. Notably, acceptable discrepancies caused by simplified evaporation and condensation model exist between experimental observations and our simulation results, such as the protrusion size, pore size, microjet speed, and keyhole depth. Further possible improvements of the computational tool are required. First, the metallic vapor is treated as a uniformly distributed gas in the keyhole pore rather a single phase. The vapor condensation is only considered in the enclosed keyhole pore, and the condensation duration

is the same as the duration of the keyhole pore collapse and splitting observed in the experiment [13]. Further incorporation of a single vapor flow is required to consider the condensation occurrence and duration based on the condensation model. Second, possible optimization strategies are proposed based on the simulation results and the literature. The proposed strategies will be discussed systematically in a future work, including the adaptive laser power strategy and the prediction strategy of the keyhole pore formation. Third, this study only considers a bare plate. Future study will be to performed to consider the presence of powder beds, which is more relevant to practical applications of L-PBF. Following the improvement of the computational tool, more quantitative analysis will be conducted to compare different scenarios and identify the most important factors that affect the instability mechanisms.

CRediT authorship contribution statement

Zhao Jidong: Writing – review & editing, Writing – original draft, Supervision, Resources, Project administration, Methodology, Investigation, Funding acquisition, Formal analysis, Conceptualization. **Yu Tao:** Writing – original draft, Visualization, Validation, Software, Methodology, Formal analysis, Data curation, Conceptualization.
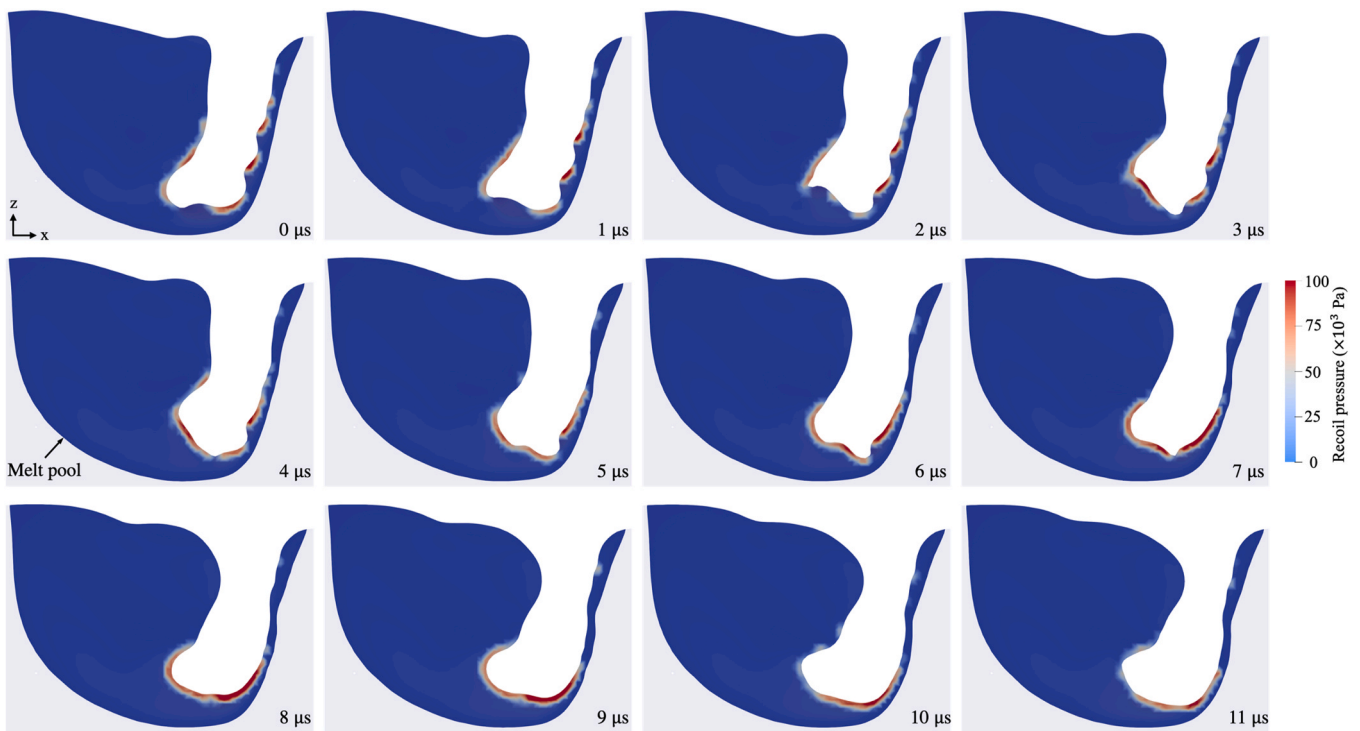
Fig. A.6. Recoil pressure contour of the central cross section at $y = 200$ μm during the formation process of the "J"-like keyhole.

Declaration of Competing Interest

The authors declare that they have no known competing financial interests or personal relationships that could have appeared to influence the work reported in this paper.

Data Availability

Data will be made available on request. The codes used to compute the results and the data that support the findings of this study are available from the corresponding author upon reasonable request.

Appendix A

Figs. A.1–A.4.
Table A.1.

Appendix B

Tables A.2 and A.3.

Appendix C

Figs. A.5 and A.6.

References

[1] Antonysamy A.A. , 2012 Microstructure, Texture and Mechanical Property Evolution during AdditiveManufacturing of Ti6Al4V Alloy for Aerospace Applications, The University of Manchester (United Kingdom),

[2] S.A. Gowers, V.F. Curto, C.A. Seneci, C. Wang, S. Anastasova, P. Vadgama, G.-Z. Yang, M.G. Boutelle, 3D printed microfluidic device with integrated biosensors for online analysis of subcutaneous human microdialysate, Anal. Chem. 87 (15) (2015) 7763–7770.

[3] J.M. Williams, A. Adewunmi, R.M. Schek, C.L. Flanagan, P.H. Krebsbach, S. E. Feinberg, S.J. Hollister, S. Das, Bone tissue engineering using polycaprolactone scaffolds fabricated via selective laser sintering, Biomaterials 26 (23) (2005) 4817–4827.

[4] L.E. Murr, S. Gaytan, F. Medina, H. Lopez, E. Martinez, B. Machado, D. Hernandez, L. Martinez, M. Lopez, R. Wicker, Next-generation biomedical implants using additive manufacturing of complex, cellular and functional mesh arrays, Philos. Trans. R. Soc., A 368 (1917) (2010) 1999–2032.

[5] J.H. Martin, B.D. Yahata, J.M. Hundley, J.A. Mayer, T.A. Schaedler, T.M. Pollock, 3D printing of high-strength aluminium alloys, Nature 549 (7672) (2017) 365–369.

[6] T. DebRoy, H. Wei, J. Zuback, T. Mukherjee, J. Elmer, J. Milewski, A.M. Beese, Ad Wilson-Heid, A. De, W. Zhang, Additive manufacturing of metallic components–process, structure and properties, Prog. Mater. Sci. 92 (2018) 112–224.

[7] D.L. Bourell, M.C. Leu, D.W. Rosen, Roadmap for additive manufacturing: identifying the future of freeform processing, Univ. Tex. Austin, Austin, TX (2009) 11–15.

[8] T. Zohdi, N. Castrillon, Variability of targeted material thermal responses to laser-induced heating in additive manufacturing, J. Manuf. Sci. Eng. 141 (8) (2019), 081012.

[9] G. Strano, L. Hao, R.M. Everson, K.E. Evans, Surface roughness analysis, modelling and prediction in selective laser melting, J. Mater. Process Technol. 213 (4) (2013) 589–597.

[10] S.A. Khairallah, A.T. Anderson, A. Rubenchik, W.E. King, Laser powder-bed fusion additive manufacturing: Physics of complex melt flow and formation mechanisms of pores, spatter, and denudation zones, Acta Mater. 108 (2016) 36–45.

[11] Thöne M. , Leuders S. , Riemer A. , Tröster T. , Richard H. , 2012 , in 2012 International Solid Freeform Fabrication Symposium. University of Texas at Austin.

[12] R. Fabbro, Melt pool and keyhole behaviour analysis for deep penetration laser welding, J. Phys. D: Appl. Phys. 43 (44) (2010), 445501.

[13] C. Zhao, N.D. Parab, X. Li, K. Fezzaa, W. Tan, A.D. Rollett, T. Sun, Critical instability at moving keyhole tip generates porosity in laser melting, Science 370 (6520) (2020) 1080–1086.

[14] S. Beretta, S. Romano, A comparison of fatigue strength sensitivity to defects for materials manufactured by AM or traditional processes, Int J. Fatigue 94 (2017) 178–191.

[15] H. Masuo, Y. Tanaka, S. Morokoshi, H. Yagura, T. Uchida, Y. Yamamoto, Y. Murakami, Influence of defects, surface roughness and HIP on the fatigue strength of Ti-6Al-4V manufactured by additive manufacturing, Int J. Fatigue 117 (2018) 163–179.

[16] K.V. Yang, P. Rometsch, T. Jarvis, J. Rao, S. Cao, C. Davies, X. Wu, Porosity formation mechanisms and fatigue response in Al-Si-Mg alloys made by selective laser melting, Mater. Sci. Eng., A 712 (2018) 166–174.

[17] L. Wang, Y. Zhang, H.Y. Chia, W. Yan, Mechanism of keyhole pore formation in metal additive manufacturing, npj Comput. Mater. 8 (1) (2022) 1–11.

[18] R. Cunningham, C. Zhao, N. Parab, C. Kantzos, J. Pauza, K. Fezzaa, T. Sun, A. D. Rollett, Keyhole threshold and morphology in laser melting revealed by ultrahigh-speed x-ray imaging, Science 363 (6429) (2019) 849–852.

[19] A. Ur Rehman, M.A. Saleem, T. Liu, K. Zhang, F. Pitir, M.U. Salamci, Influence of silicon carbide on direct powder bed selective laser process (sintering/melting) of alumina, Mater 15 (2) (2022) 637.

[20] W.E. King, H.D. Barth, V.M. Castillo, G.F. Gallegos, J.W. Gibbs, D.E. Hahn, C. Kamath, A.M. Rubenchik, Observation of keyhole-mode laser melting in laser powder-bed fusion additive manufacturing, J. Mater. Process Technol. 214 (12) (2014) 2915–2925.

[21] Q. Guo, C. Zhao, M. Qu, L. Xiong, S.M.H. Hojjatzadeh, L.I. Escano, N.D. Parab, K. Fezzaa, T. Sun, L. Chen, In-situ full-field mapping of melt flow dynamics in laser metal additive manufacturing, Addit. Manuf. 31 (2020), 100939.

[22] Z.A. Young, Q. Guo, N.D. Parab, C. Zhao, M. Qu, L.I. Escano, K. Fezzaa, W. Everhart, T. Sun, L. Chen, Types of spatter and their features and formation mechanisms in laser powder bed fusion additive manufacturing process, Addit. Manuf. 36 (2020), 101438.

[23] Q. Guo, M. Qu, L.I. Escano, S.M.H. Hojjatzadeh, Z. Young, K. Fezzaa, L. Chen, Revealing melt flow instabilities in laser powder bed fusion additive manufacturing of aluminum alloy via in-situ high-speed X-ray imaging, Int J. Mach. Tools Manuf. 175 (2022), 103861.

[24] Q. Guo, C. Zhao, L.I. Escano, Z. Young, L. Xiong, K. Fezzaa, W. Everhart, B. Brown, T. Sun, L. Chen, Transient dynamics of powder spattering in laser powder bed fusion additive manufacturing process revealed by in-situ high-speed high-energy x-ray imaging, Acta Mater. 151 (2018) 169–180.

[25] A. Ur Rehman, M.A. Mahmood, P. Ansari, F. Pitir, M.U. Salamci, A.C. Popescu, I. N. Mihailescu, Spatter formation and splashing induced defects in laser-based powder bed fusion of AlSi10Mg alloy: a novel hydrodynamics modelling with empirical testing, Metals 11 (12) (2021) 2023.

[26] C. Zhao, Q. Guo, X. Li, N. Parab, K. Fezzaa, W. Tan, L. Chen, T. Sun, Bulk-explosion-induced metal spattering during laser processing, Phys. Rev. X 9 (2) (2019), 021052.

[27] A. Ullah, A. Ur Rehman, M.U. Salamci, F. Pıtır, T. Liu, The influence of laser power and scanning speed on the microstructure and surface morphology of Cu2O parts in SLM, Rapid Prototyp. J. 28 (9) (2022) 1796–1807.

[28] Y. Huang, T.G. Fleming, S.J. Clark, S. Marussi, K. Fezzaa, J. Thiyagalingam, C.L. A. Leung, P.D. Lee, Keyhole fluctuation and pore formation mechanisms during laser powder bed fusion additive manufacturing, Nat. Commun. 13 (1) (2022) 1–11.

[29] S.M.H. Hojjatzadeh, N.D. Parab, W. Yan, Q. Guo, L. Xiong, C. Zhao, M. Qu, L. I. Escano, X. Xiao, K. Fezzaa, Pore elimination mechanisms during 3D printing of metals, Nat. Commun. 10 (1) (2019) 1–8.

[30] Q. Guo, C. Zhao, M. Qu, L. Xiong, L.I. Escano, S.M.H. Hojjatzadeh, N.D. Parab, K. Fezzaa, W. Everhart, T. Sun, In-situ characterization and quantification of melt pool variation under constant input energy density in laser powder bed fusion additive manufacturing process, Addit. Manuf. 28 (2019) 600–609.

[31] S.M.H. Hojjatzadeh, N.D. Parab, Q. Guo, M. Qu, L. Xiong, C. Zhao, L.I. Escano, K. Fezzaa, W. Everhart, T. Sun, Direct observation of pore formation mechanisms during LPBF additive manufacturing process and high energy density laser welding, Int J. Mach. Tools Manuf. 153 (2020), 103555.

[32] M. Qu, Q. Guo, L.I. Escano, S.J. Clark, K. Fezzaa, L. Chen, Mitigating keyhole pore formation by nanoparticles during laser powder bed fusion additive manufacturing, Addit. Manuf. Lett. 3 (2022), 100068.

[33] A.M. Kiss, A.Y. Fong, N.P. Calta, V. Thampy, A.A. Martin, P.J. Depond, J. Wang, M.J. Matthews, R.T. Ott, C.J. Tassone, Laser-induced keyhole defect dynamics during metal additive manufacturing, Adv. Eng. Mater. 21 (10) (2019), 1900455.

[34] C. Zhao, K. Fezzaa, R.W. Cunningham, H. Wen, F. De Carlo, L. Chen, A.D. Rollett, T. Sun, Real-time monitoring of laser powder bed fusion process using high-speed X-ray imaging and diffraction, Sci. Rep. 7 (1) (2017) 1–11.

[35] C. Zhao, B. Shi, S. Chen, D. Du, T. Sun, B.J. Simonds, K. Fezzaa, A.D. Rollett, Laser melting modes in metal powder bed fusion additive manufacturing, Rev. Mod. Phys. 94 (4) (2022), 045002.

[36] S.A. Khairallah, A.A. Martin, J.R. Lee, G. Guss, N.P. Calta, J.A. Hammons, M. H. Nielsen, K. Chaput, E. Schwalbach, M.N. Shah, Controlling interdependent meso-nanosecond dynamics and defect generation in metal 3D printing, Science 368 (6491) (2020) 660–665.

[37] H. Chen, W. Yan, Spattering and denudation in laser powder bed fusion process: Multiphase flow modelling, Acta Mater. 196 (2020) 154–167.

[38] T. Sun, Probing Ultrafast dynamics in laser powder bed fusion using high-speed x-ray imaging: a review of research at the advanced photon source, Jom 72 (3) (2020) 999–1008.

[39] R. Ganeriwala, T.I. Zohdi, A coupled discrete element-finite difference model of selective laser sintering, Granul. Matter 18 (2) (2016) 21.

[40] R. Lin, H.-p Wang, F. Lu, J. Solomon, B.E. Carlson, Numerical study of keyhole dynamics and keyhole-induced porosity formation in remote laser welding of Al alloys, Int J. Heat. Mass Transf. 108 (2017) 244–256.

[41] C. Tang, J.L. Tan, C.H. Wong, A numerical investigation on the physical mechanisms of single track defects in selective laser melting, Int J. Heat. Mass Transf. 126 (2018) 957–968.

[42] P. Tan, R. Kiran, K. Zhou, Effects of sub-atmospheric pressure on keyhole dynamics and porosity in products fabricated by selective laser melting, J. Manuf. Process 64 (2021) 816–827.

[43] K. Le, C. Tang, C. Wong, On the study of keyhole-mode melting in selective laser melting process, Int J. Therm. Sci. 145 (2019), 105992.

[44] M. Bayat, A. Thanki, S. Mohanty, A. Witvrouw, S. Yang, J. Thorborg, N.S. Tiedje, J.H. Hattel, Keyhole-induced porosities in laser-based powder bed fusion (L-PBF) of Ti6Al4V: High-fidelity modelling and experimental validation, Addit. Manuf. 30 (2019), 100835.

[45] A.A. Martin, N.P. Calta, S.A. Khairallah, J. Wang, P.J. Depond, A.Y. Fong, V. Thampy, G.M. Guss, A.M. Kiss, K.H. Stone, Dynamics of pore formation during laser powder bed fusion additive manufacturing, Nat. Commun. 10 (1) (2019) 1–10.

[46] H. Zhou, H. Su, Y. Guo, P. Yang, Y. Liu, Z. Shen, D. Zhao, H. Liu, T. Huang, M. Guo, Formation and evolution mechanisms of pores in Inconel 718 during selective laser melting: Meso-scale modeling and experimental investigations, J. Manuf. Process 81 (2022) 202–213.

[47] A. Ur Rehman, M.A. Mahmood, F. Pitir, M.U. Salamci, A.C. Popescu, I. N. Mihailescu, Keyhole formation by laser drilling in laser powder bed fusion of Ti6Al4V biomedical alloy: Mesoscopic computational fluid dynamics simulation versus mathematical modelling using empirical validation, Nanomate 11 (12) (2021) 3284.

[48] Y. Yang, O. Ragnvaldsen, Y. Bai, M. Yi, B.-X. Xu, 3D non-isothermal phase-field simulation of microstructure evolution during selective laser sintering, npj Comput. Mater. 5 (1) (2019) 1–12.

[49] A.J. Pinkerton, An analytical model of beam attenuation and powder heating during coaxial laser direct metal deposition, J. Phys. D: Appl. Phys. 40 (23) (2007) 7323.

[50] T. Yu, J. Zhao, Semi-coupled resolved CFD–DEM simulation of powder-based selective laser melting for additive manufacturing, Comput. Methods Appl. Mech. Engrg 377 (2021), 113707.

[51] T. Yu, J. Zhao, Quantitative simulation of selective laser melting of metals enabled by new high-fidelity multiphase, multiphysics computational tool, Comput. Methods Appl. Mech. Engrg 399 (2022), 115422.

[52] Z. Wang, W. Yan, W.K. Liu, M. Liu, Powder-scale multi-physics modeling of multi-layer multi-track selective laser melting with sharp interface capturing method, Comput. Mech. 63 (4) (2019) 649–661.

[53] C. Qiu, C. Panwisawas, M. Ward, H.C. Basoalto, J.W. Brooks, M.M. Attallah, On the role of melt flow into the surface structure and porosity development during selective laser melting, Acta Mater. 96 (2015) 72–79.

[54] C. Panwisawas, C. Qiu, Y. Sovani, J. Brooks, M. Attallah, H. Basoalto, On the role of thermal fluid dynamics into the evolution of porosity during selective laser melting, Scr. Mater. 105 (2015) 14–17.

[55] J. Roenby, H. Bredmose, H. Jasak, A computational method for sharp interface advection, R. Soc. Open Sci. 3 (11) (2016), 160405.

[56] M. Rudman, Volume-tracking methods for interfacial flow calculations, Int J. Numer. Methods Fluids 24 (7) (1997) 671–691.

[57] M. Rudman, A volume-tracking method for incompressible multifluid flows with large density variations, Int J. Numer. Methods Fluids 28 (2) (1998) 357–378.

[58] L. Wang, Y. Zhang, W. Yan, Evaporation model for keyhole dynamics during additive manufacturing of metal, Phys. Rev. Appl. 14 (6) (2020), 064039.

[59] S. Anisimov, in 30 Years of the Landau Institute-Selected Papers, 11, World Scientific,, Singapore, 1996, p. 14.

[60] M. Knudsen, Die maximale verdampfungsgeschwindigkeit des quecksilbers, Ann. der Phys. 352 (13) (1915) 697–708.

[61] D. Sun, J. Xu, Q. Chen, Modeling of the evaporation and condensation phase-change problems with FLUENT. Numer Heat Transfer, Part B 66 (4) (2014) 326–342.

[62] A. Badillo, Quantitative phase-field modeling for boiling phenomena, Phys. Rev. E 86 (4) (2012), 041603.

[63] A.A. Badillo, in ASME International Mechanical Engineering Congress and Exposition, vol. 56369, American Society of Mechanical Engineers,, 2013 pp. V08CT09A064.

[64] R. Szijártó, A. Badillo, B. Ničeno, H.-M. Prasser, Condensation models for the water–steam interface and the volume of fluid method, Int J. Multiph. Flow. 93 (2017) 63–70.

[65] R. Swanepoel, Determination of the thickness and optical constants of amorphous silicon, J. Phys. E: Sci. Instrum. 16 (12) (1983) 1214.

[66] M.S. William, M. Jyotirmoy, Laser material processing, Steen Springe -Verl., Lond., Berl., Heidelb. 3 (2010) 408.

[67] J. Tan, C. Tang, C. Wong, Study and modeling of melt pool evolution in selective laser melting process of SS316L, MRS Commun. 8 (3) (2018) 1178–1183.

[68] Saldi Z.S. (2012) Marangoni driven free surface flows in liquid weld pools.

[69] J.U. Brackbill, D.B. Kothe, C. Zemach, A continuum method for modeling surface tension, J. Comput. Phys. 100 (2) (1992) 335–354.

[70] C. Panwisawas, C. Qiu, M.J. Anderson, Y. Sovani, R.P. Turner, M.M. Attallah, J. W. Brooks, H.C. Basoalto, Mesoscale modelling of selective laser melting: Thermal fluid dynamics and microstructural evolution, Comput. Mater. Sci. 126 (2017) 479–490.

[71] J. Tan, C. Tang, C. Wong, Study and modeling of melt pool evolution in selective laser melting process of SS316L, MRS Commun. 8 (2018) 1178–1183.

[72] J.-H. Cho, D.F. Farson, J.O. Milewski, K.J. Hollis, Weld pool flows during initial stages of keyhole formation in laser welding, J. Phys. D: Appl. Phys. 42 (17) (2009), 175502.

[73] R.I. Issa, Solution of the implicitly discretised fluid flow equations by operator-splitting, J. Comput. Phys. 62 (1) (1986) 40–65.

[74] Saldi Z.S. , 2012 , Marangoni driven free surface flows in liquid weld pools [thesis]. Delft: Department of Multi Scale Physics, Faculty of Applied Sciences. Delft University of Technology.

[75] Valencia J.J. , Quested P.N. , 2013 , Thermophysical properties.

[76] S. Ly, A.M. Rubenchik, S.A. Khairallah, G. Guss, M.J. Matthews, Metal vapor micro-jet controls material redistribution in laser powder bed fusion additive manufacturing, Sci. Rep. 7 (1) (2017) 4085.

[77] X. Li, C. Zhao, T. Sun, W. Tan, Revealing transient powder-gas interaction in laser powder bed fusion process through multi-physics modeling and high-speed synchrotron x-ray imaging, Addit. Manuf. 35 (2020), 101362.

[78] A.A. Martin, N.P. Calta, S.A. Khairallah, J. Wang, P.J. Depond, A.Y. Fong, V. Thampy, G.M. Guss, A.M. Kiss, K.H. Stone, Dynamics of pore formation during laser powder bed fusion additive manufacturing, Nat. Commun. 10 (1) (2019) 1987.

[79] C.L.A. Leung, S. Marussi, R.C. Atwood, M. Towrie, P.J. Withers, P.D. Lee, In situ X-ray imaging of defect and molten pool dynamics in laser additive manufacturing, Nat. Commun. 9 (1) (2018) 1355.

[80] Y. Zhang, G.S. Hong, D. Ye, K. Zhu, J.Y. Fuh, Extraction and evaluation of melt pool, plume and spatter information for powder-bed fusion AM process monitoring, Mater. Des. 156 (2018) 458–469.

[81] I. Yadroitsev, A. Gusarov, I. Yadroitsava, I. Smurov, Single track formation in selective laser melting of metal powders, J. Mater. Process Technol. 210 (12) (2010) 1624–1631.

[82] J. Yin, D. Wang, L. Yang, H. Wei, P. Dong, L. Ke, G. Wang, H. Zhu, X. Zeng, Correlation between forming quality and spatter dynamics in laser powder bed fusion, Addit. Manuf. 31 (2020), 100958.

[83] Q.C. Liu, J. Elambasseril, S.J. Sun, M. Leary, M. Brandt, P.K. Sharp, Advanced materials research, Trans. Tech. Publ. vol. 891 (2014) 1519–1524.

[84] X. Li, Q. Guo, L. Chen, W. Tan, Quantitative investigation of gas flow, powder-gas interaction, and powder behavior under different ambient pressure levels in laser powder bed fusion, Int J. Mach. Tools Manuf. 170 (2021), 103797.

[85] N. Kouraytem, X. Li, R. Cunningham, C. Zhao, N. Parab, T. Sun, A.D. Rollett, A. D. Spear, W. Tan, Effect of laser-matter interaction on molten pool flow and keyhole dynamics, Phys. Rev. Appl. 11 (6) (2019), 064054.

[86] T. Montalbano, B.N. Briggs, J.L. Waterman, S. Nimer, C. Peitsch, J. Sopcisak, D. Trigg, S. Storck, Uncovering the coupled impact of defect morphology and microstructure on the tensile behavior of Ti-6Al-4V fabricated via laser powder bed fusion, J. Mater. Process Technol. 294 (2021), 117113.

[87] Ľ. Straka, J. Piteľ, I. Čorný, Influence of the main technological parameters and material properties of the workpiece on the geometrical accuracy of the machined surface at wedm, Int J. Adv. Manuf. Technol. 115 (9–10) (2021) 3065–3087.

[88] A.V. Panin, M.S. Kazachenok, S.V. Panin, F. Berto, Scale levels of quasi-static and dynamic fracture behavior of Ti-6Al-4V parts built by various additive manufacturing methods, Theor. Appl. Fract. Mech. 110 (2020), 102781.

[89] M. Colombo, M. Colombo, Regularity results for very degenerate elliptic equations, Flows Non-Smooth Vector Fields Degenerate Elliptic Equ.: Appl. Vlasov-Poisson Semigeostrophic Syst. (2017) 119–157.

[90] N.T. Aboulkhair, N.M. Everitt, I. Ashcroft, C. Tuck, Reducing porosity in AlSi10Mg parts processed by selective laser melting, Addit. Manuf. 1 (2014) 77–86.

[91] J.-B. Forien, N.P. Calta, P.J. DePond, G.M. Guss, T.T. Roehling, M.J. Matthews, Detecting keyhole pore defects and monitoring process signatures during laser powder bed fusion: a correlation between in situ pyrometry and ex situ X-ray radiography, Addit. Manuf. 35 (2020), 101336.

[92] J.D. Anderson, McGraw-Hill series in aeronautical and aerospace engineering, Fundam. Aerodyn. (2003) 54–56.

[93] Z. Ren, L. Gao, S.J. Clark, K. Fezzaa, P. Shevchenko, A. Choi, W. Everhart, A. D. Rollett, L. Chen, T. Sun, Machine learning-aided real-time detection of keyhole pore generation in laser powder bed fusion, Science 379 (6627) (2023) 89–94.

[94] T. Watanabe, Y. Kukita, Translational and radial motions of a bubble in an acoustic standing wave field, Phys. Fluids A 5 (11) (1993) 2682–2688.

[95] G. Sankin, W. Simmons, S. Zhu, P. Zhong, Shock wave interaction with laser-generated single bubbles, Phys. Rev. Lett. 95 (3) (2005), 034501.

[96] C. Todaro, M. Easton, D. Qiu, D. Zhang, M. Bermingham, E. Lui, M. Brandt, D. StJohn, M. Qian, Grain structure control during metal 3D printing by high-intensity ultrasound, Nat. Commun. 11 (1) (2020) 142.

[97] A. Leipertz, A.P. Fröba, Improvement of condensation heat transfer by surface modifications, Heat. Transf. Eng. 29 (4) (2008) 343–356.

[98] M. Rausch, A. Leipertz, A. Fröba, Dropwise condensation of steam on ion implanted titanium surfaces, Int J. Heat. Mass Transf. 53 (1–3) (2010) 423–430.

[99] J. Reijonen, A. Revuelta, T. Riipinen, K. Ruusuvuori, P. Puukko, On the effect of shielding gas flow on porosity and melt pool geometry in laser powder bed fusion additive manufacturing, Addit. Manuf. 32 (2020), 101030.

[100] Wirth F., Frauchiger A., Gutknecht K., Cloots M. , 2021 in Industrializing Additive Manufacturing: Proceedings of AMPA2020. Springer: pp. 192–204.

[101] P. Wen, Y. Qin, Y. Chen, M. Voshage, L. Jauer, R. Poprawe, J.H. Schleifenbaum, Laser additive manufacturing of Zn porous scaffolds: shielding gas flow, surface quality and densification, J. Mater. Sci. Technol. 35 (2) (2019) 368–376.

[102] X. Zhang, B. Cheng, C. Tuffile, Simulation study of the spatter removal process and optimization design of gas flow system in laser powder bed fusion, Addit. Manuf. 32 (2020), 101049.

[103] Y. Yang, Z. Chen, Z. Liu, H. Wang, Y. Zhang, D. Wang, Influence of shielding gas flow consistency on parts quality consistency during large-scale laser powder bed fusion, Opt. Laser Technol. 158 (2023), 108899.

[104] S. Katayama, Y. Kawahito, M. Mizutani, Elucidation of laser welding phenomena and factors affecting weld penetration and welding defects, Phys. Procedia 5 (2010) 9–17.

[105] J. Zou, W. Yang, S. Wu, Y. He, R. Xiao, Effect of plume on weld penetration during high-power fiber laser welding, J. Laser Appl. 28 (2) (2016), 022003.

[106] Kong C.-J. , Tuck C.J. , Ashcroft I.A. , Wildman R.D. , Hague R. , 2011 , in 2011 International Solid Freeform Fabrication Symposium. University of Texas at Austin.

[107] B. Ferrar, L. Mullen, E. Jones, R. Stamp, C. Sutcliffe, Gas flow effects on selective laser melting (SLM) manufacturing performance, J. Mater. Process Technol. 212 (2) (2012) 355–364.

[108] A. Ladewig, G. Schlick, M. Fisser, V. Schulze, U. Glatzel, Influence of the shielding gas flow on the removal of process by-products in the selective laser melting process, Addit. Manuf. 10 (2016) 1–9.

[109] A.B. Anwar, Q.-C. Pham, Selective laser melting of AlSi10Mg: effects of scan direction, part placement and inert gas flow velocity on tensile strength, J. Mater. Process Technol. 240 (2017) 388–396.

[110] N. Young, J.S. Goldstein, M. Block, The motion of bubbles in a vertical temperature gradient, J. Fluid Mech. 6 (3) (1959) 350–356.

[111] T. Bergman, J. Keller, Combined buoyancy, surface tension flow in liquid metals, Numer. Heat. Transf. 13 (1) (1988) 49–63.

[112] Sasmal G. , Hochstein J. , 1994 , Marangoni convection with a curved and deforming free surface in a cavity.

[113] Francois M.M. , Sicilian J.M. , Kothe D.B. , 2006, Modeling of thermocapillary forces within a volume tracking algorithm. Modeling of Casting, Welding and Advanced Solidification Processes–XI, Opio, France, May:935–942.

[114] A.K. Sen, S.H. Davis, Steady thermocapillary flows in two-dimensional slots, J. Fluid Mech. 121 (1982) 163–186.

[115] L. Tan, S. Leong, E. Leonardi, T. Barber, A numerical study of solid-liquid phase change with Marangoni effects using a multiphase approach, Prog. Comput. Fluid Dyn., Int. J. 6 (6) (2006) 304–313.